A crack-opening-dependent numerical model for self-healing cementitious materials

A.D. Jefferson [*], B.L. Freeman

Cardiff University School of Engineering. The Parade, Cardiff CF24 3AA, UK

A R T I C L E   I N F O

A B S T R A C T

A new damage-healing model for self-healing cementitious materials is described. The model is formulated using results from a discrete ligament model and guided by the findings of a linked experimental study. Healing is simulated using the interaction of curing fronts propagating from opposing crack faces within a body of healing-agent. This approach accounts for the dependency of the healing response on the crack opening displacement (COD) and its rate. The new damage-healing cohesive-zone model is applied to an element with an embedded strong-discontinuity within a coupled finite-element code, which simulates healing-agent transport and mechanical behaviour. The model is validated using data from tests with different CODs and COD rates. The validations show that the coupled model represents the mechanical and flow behaviour of an autonomic self-healing system with good accuracy for a range of cracking configurations and load paths.

1. Introduction

Biomimetic construction materials with the ability to self-heal are being developed so that future structures do not suffer from the cracking-related durability problems that have afflicted a significant proportion of our existing infrastructure (Gardner et al., 2018). The potential of these materials 'to deliver major change, most noticeably in the built environment' has been highlighted in a recent Royal Society report (The Royal Society, 2021). Numerical models can play an important role in the development of biomimetic materials because, once calibrated, they allow a larger parameter space to be investigated than is practicable with experimentation and they permit materials to be tailored to specific applications. In addition, the ability to simulate the cracking and healing behaviour of self-healing cementitious materials is important when designing structures formed from these materials (Jefferson et al., 2018). Such simulations should address the size and disposition of cracks, healing time and healing efficiency, changes in permeability, and load–displacement responses, all of which are important considerations in the design of this type of cementitious structure.

This work focusses on the simulation of autonomic self-healing cementitious materials (SHCMs) with embedded healing-agents (Van Tittelboom and De Belie, 2013; De Belie et al., 2018; Xue et al., 2019), but the processes studied and the new relationships developed in this work are relevant to a wide range of biomimetic materials and healing systems.

Early self-healing (SH) material models considered only mechanical behaviour (Barbero et al., 2005; Schimmel and Remmers, 2006; Granger et al., 2007) and nearly all of these, as well as many more recent contributions, were based on continuum damage mechanics (CDM) (Lemaitre and Desmorat, 2005). CDM is a natural choice for SH material models because the damage variables used in these formulations provide convenient measures of the material available for healing. The extended theory has been named 'continuum damage healing mechanics' (CDHM) and models based on this framework normally use a healing variable (or tensor) as a multiplier on the damaged portion of material (Darabi et al., 2012; Pan et al., 2018). CDHM theories have also been applied in micromechanical formulations (Davies and Jefferson, 2017), which are particularly well-suited to the simulation of SHCMs containing microcapsules (Han et al., 2021).

Thermodynamic principles underpin most damage formulations, with constitutive relationships normally derived from thermodynamic free-energy potentials such that models always predict non-negative energy dissipation (Lemaitre and Desmorat, 2005). The same basic principles are used in CDHM except that thermodynamic potentials are expanded to incorporate one or more healing variable(s) (Barbero et al., 2005; Voyiadjis et al., 2012; Alsheghri and Abu Al-Rub, 2015). An important thermodynamic aspect of the healing process is that, in
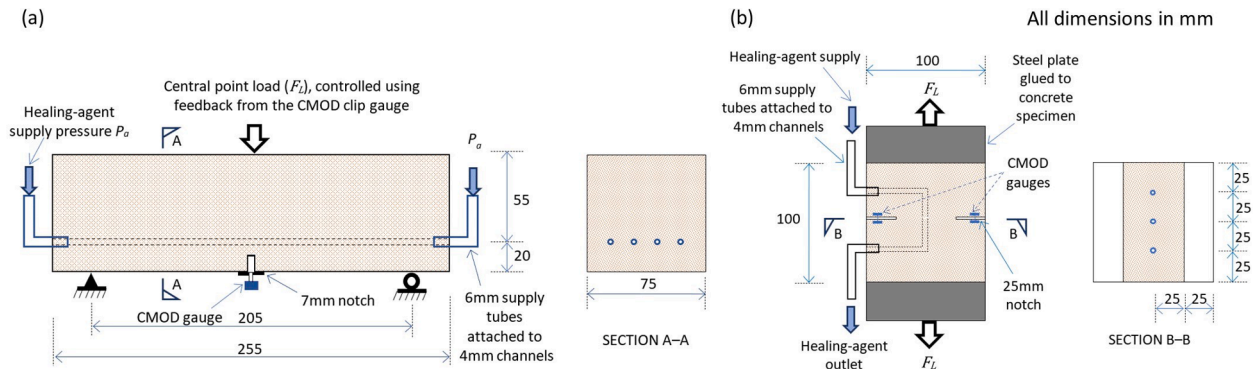

Fig. 1. Experimental arrangement for (a) SF and SO test series, and (b) DT test series.

contrast to damage, it does not dissipate mechanical energy since healing-agents normally cure within cracks in a nominally stress-free state. This implies that under isothermal constant-strain conditions, the recovery of stiffness due to healing causes no change in either the stress or mechanical energy state within the surrounding continuum. Furthermore, when healing occurs under non-zero strain conditions, a permanent 'healing' strain develops that is associated with the hardening of healing-agents in micro-cracks (Mergheim and Steinmann, 2013; Davies and Jefferson, 2017; Jefferson et al., 2018).

A range of approaches has been used for simulating time-dependent healing. Some models treat healing as a similar process to damage that develops according to a thermodynamic driving force (Barbero et al., 2005; Voyiadjis et al., 2011). A number of investigators have employed rate dependent healing approaches (Voyiadjis et al., 2011; Darabi et al., 2012), while others have developed time dependent exponential healing functions (Mergheim and Steinmann, 2013; Oucif et al., 2018). Wool and O'Connor (1981) introduced a recovery variable based on a convolution integral in their polymer healing model. Mergheim and Steinmann (2013) also derived a convolution integral from their exponential healing function and developed a convenient two-level recursive scheme for evaluating healing variables in a transient analysis. These different approaches reflect variations in the host material, healing systems, healing-agents and the loading scenarios considered.

CDHM is applicable to the formation and healing of micro-cracks and is well-suited to SH materials with embedded micro-capsules that contain healing-agents (White et al., 2001; De Belie et al., 2018). Alternative self-healing systems, with embedded hollow fibres (Dry, 1994; Van Tittelboom and De Belie, 2013), brittle tubes (Joseph et al., 2010; Van Belleghem et al., 2018) or interconnected vascular networks (Minnebo et al., 2017; De Nardi et al., 2020), are used for healing macro-cracks, since larger volumes of healing-agent are required to fill such cracks. The simulation of these SH material systems requires an approach that represents macro-cracks and their healing. Most SH models for discrete cracks use cohesive crack idealisations based on damage-healing formulations (Caggiano et al., 2017), which have a similar form to their CDHM counterparts. These models have been incorporated in finite element codes using discrete elements (Zhou et al., 2017), elements with embedded strong discontinuities (Zhang and Zhuang, 2018; Freeman et al., 2020) and the extended finite element method (Gilabert et al., 2017a; Gilabert et al., 2017b).

In all of the self-healing materials discussed above, the healing process involves autonomic healing compounds being transported to crack sites and subsequently curing within micro- or macro-cracks. Relatively few attempts have been made to simulate the associated flow processes (Jefferson et al., 2018; Mauludin and Oucif, 2019), although Gilabert et al. (2017a) and Gilabert et al. (2017b) simulated the flow of a polyurethane-based healing-agent into a concrete crack using computational fluid dynamics and Gardner et al. (2014, 2017) used a modified Lucas-Washburn equation to model the flow of healing-agents in discrete cracks.

In this paper, the only damage process considered is cracking due to mechanical loading, thus the terms damage and cracking are used synonymously.

The primary purpose of this article is to present a new damage-healing model for simulating healing in both static cracks and in cracks with transient crack opening displacements (CODs). The paper describes how results from a one-dimensional ligament model were used to determine the governing relationships of a homogenised model that simulates the behaviour of a representative zone of material. The novelty of the model lies in the way that, (i) homogenised damage and healing variables evolve to represent interspersed damaged and healed material, (ii) healing is simulated using the interaction between diffuse curing fronts emanating from opposing crack faces with a COD rate dependent factor, and (iii) generalised curing front variables are accumulated and updated when re-damage and re-healing occur. The model simulates the strong dependency of healing on the COD and its rate, and places no restrictions on the timing or rate of cracking or healing. This is important because cracks are rarely inanimate during healing, and any movement of the crack boundaries affects the healing process. Furthermore, cracks in almost all applications vary greatly in their dimensions as well as the rate at which they open and close during healing. The degree of healing and rate of healing can change by orders of magnitude with the COD or COD rate. Thus, models that assume instantaneous healing or use a single healing rate function with no allowance for the COD or its rate can give very inaccurate results. In addition, models that assume that healing and cracking processes always occur over separate discrete time intervals are very restricted in the range of problems that they can simulate accurately (Jefferson et al., 2018).

The development of the new damage-healing cohesive zone model described herein formed part of a wider programme of work on the characterisation and modelling of SHCMs. This work included an experimental study on the transport and mechanical processes that govern the behaviour of SHCMs (Selvarajoo et al., 2020a; 2020b); the development of a computational transport model (Freeman and Jefferson, 2020) (Appendix C) to describe the release, flow and curing of healing-agents in the cracked cementitious host material; and the derivation and implementation a specialised finite element with an embedded strong-discontinuity (Freeman et al., 2020). It is noted that the constitutive model presented in outline in the latter article was a considerably simplified version of the model presented in this paper that did not fully account for COD or COD rate effects. The coupled finite element model formed from the components described in (Freeman and Jefferson, 2020) and (Freeman et al., 2020), along with the new damage-healing model described herein, was used for the simulations reported in this article. Although our models were developed using data from a specific SHCM, the modelling approach should be applicable to a wide range of self-healing systems and materials.

Table 1
Summary of experiments considered with the model.

Designation	Type of specimen and loading	Crack condition during healing period
SF	Notched beam under 3 point loading (Fig. 1a)	Tapering crack, fixed during the healing period CMOD = 0.15 mm and t_f = 120 s [see Notes]
SO	Notched beam under 3 point loading (Fig. 1a)	Tapering crack opening during the healing period with CMOD rates of: Set 1: 0.0005 mm/s, Set 2: 0.001 mm/s, Set 3: 0.002 mm/s
DT	Notched cube loaded in direct tension (Fig. 1b)	Nominally uniform crack fixed during the healing period with CODs and healing periods of: DT1: COD = 0.1 mm: t_f = 60 s and 600 s DT2: COD = 0.2 mm: t_f = 60 s and 1200 s

Notes: t_f = healing period: CMOD = Crack Mouth Opening Displacement.

In the remainder of this paper, the autonomic system used in this study and the associated governing processes are described, along with other preliminary and background information (Section 2). The homogenised damage-healing model and its derivation from a set of one-dimensional discrete ligament model simulations is explained (Section 3). An approach for computing the healing parameter from interacting curing fronts is presented (Section 4). An overall solution framework is described and details of the algorithm used to implement the damage-healing formulation in a cohesive zone model are given (Section 5). A set of examples is presented that evaluates the ability of the coupled model to represent the transport and mechanical behaviour of SHCM specimens for a range of transient loading conditions. The sensitivity of the predicted response to variations in the damage-healing model's material properties is also shown (Section 6). The main conclusions from the work are then given (Section 7). A proof of the thermodynamic validity of the formulation and details of the transport model are provided in the Appendices.

2. Preliminaries

2.1. Autonomic healing system and experimental observations.

We studied the processes that govern the behaviour of an autonomic cementitious self-healing system in a series of experiments (Selvarajoo et al., 2020a, 2020b). The system studied comprised a vascular network embedded in concrete specimens with PC20 cyanoacrylate (CA) as the healing-agent. CA was chosen because it is a relatively fast acting agent that allowed us to study simultaneous cracking–healing processes in tests of modest duration (i.e. 1–30 min).

The experiments undertaken to study the mechanical behaviour (Selvarajoo et al., 2020a) of the system included notched beam tests (SF and SO series, see Fig. 1a) and direct tension tests on doubly notched cube specimens (DT1 and DT2 series, Fig. 1b). The experimental procedures for these tests are outlined in Section 6. The SF and DT series were designed so that healing took place under fixed crack conditions. By contrast, the COD increased at a constant rate in the SO series tests so that cracking and healing occurred simultaneously. A summary of the tests considered in Section 6 is given in Table 1.

The experimental programme of tests used to study the transport and curing characteristics of the system (Selvarajoo et al., 2020b) considered the capillary flow behaviour of CA in static macro-cracks, the sorption of CA into concrete specimens through natural crack surfaces, the development and progress of CA curing fronts adjacent to a concrete substrate and the dynamic flow characteristics of CA in capillary channels. These transport and curing experiments, as well as those undertaken by others (Ferrara et al., 2018), showed that healing-agent is released from supply channels, flows into the crack and surrounding micro-cracked zone, and then cures gradually. The experiments showed that a curing front develops in the body of healing-agent adjacent to each crack wall, and then progresses towards the centre of the crack, with the curing front becoming more diffuse over time, as explained in Section 4.

2.2. Flow and curing processes

In Freeman and Jefferson (2020) we presented a transport and curing model for this healing system that was used for the simulations reported in Section 6. The transport component of the model is summarised in Appendix C. The curing model component simulates a polymerisation reaction which is initiated by hydroxide ions that are transported from the cementitious substrate into and through the body of CA via a diffusion process. The rate of progress of the polymerisation, or *curing*, front gradually slows as the cured material forms an increasingly impermeable barrier to the further migration of OH⁻ ions (Tomlinson et al., 2006). We showed that the mean position of the curing front ($z_f(t_c)$) at curing time t_c is well represented by the following equation:

$$z_f(t_c) = z_{c0}\left(1 - e^{-t_c/\tau}\right) \tag{1}$$

where z_{c0} is the critical curing depth and τ is the curing time parameter.

By solving an advection–diffusion equation for the degree of cure
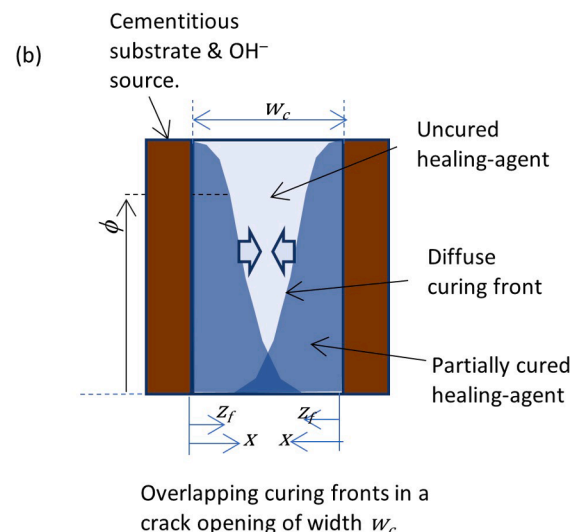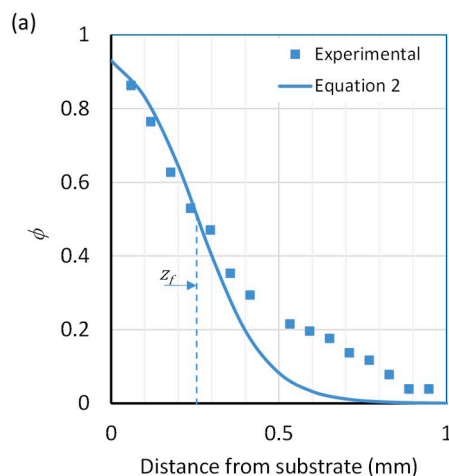
Fig. 2. (a) Comparison between Eq. (2) and experimental data. (b) Schematic showing symmetric curing fronts within a crack filled with healing-agent.
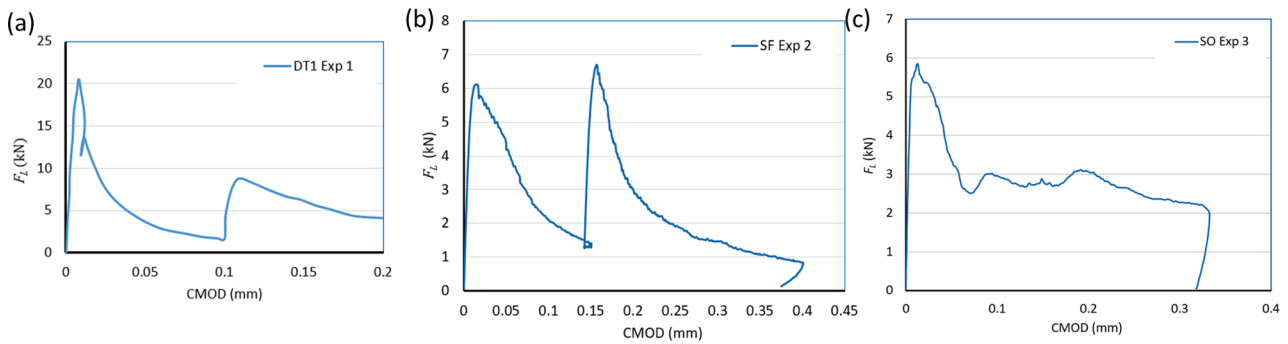
Fig. 3. Typical load-CMOD responses from (a) DT, (b) SF and (c) SO series tests (Selvarajoo et al., 2020a).

(ϕ), we showed that the distribution of ϕ across a crack may be simulated with the following equation:

$$\phi(x, z_f) = \frac{1}{2}\left(1 - tanh\left(\frac{x - z_f - z_{c2}}{z_{c2} + \sqrt{z_f/z_{c1}}}\right)\right) \tag{2}$$

where x is defined in Fig. 2, z_{c1} is the curing front constant and z_{c2} is the wall factor.

Fig. 2a shows a comparison between a predicted ϕ distribution obtained using (2) and measured values obtained from the curing front experiments described in Selvarajoo et al. (2020b). The parameters used in the comparison shown in Fig. 2a and further background to the curing front function is provided in Appendix C. A schematic diagram illustrating diffuse curing fronts progressing from opposing crack faces is presented in Fig. 2b. Throughout this work we have assumed that, within a filled crack, opposing curing fronts are symmetric.

2.3. Observed mechanical behaviour and applicability of damage mechanics

Fig. 3 shows characteristic responses from the beam and direct tension tests in which cracks had fixed CODs during the healing period (DT and SF series), and from beam tests that maintained a constant CMOD rate during healing (SO series). The former (Fig. 3a and b) show that the re-cracking response of healed specimens has the same characteristic softening behaviour as that of the virgin material, although the plots also show that the peak strength and fracture energy of the virgin and healed material can be markedly different from each other. It is well-known that this type of fracture response can be replicated with a cohesive-zone damage model (Elices et al., 2002; De Borst et al., 2012).

The responses of the SO specimens were very different from those of the fixed crack tests, as illustrated in Fig. 3c. In these specimens, cracking and healing progressed simultaneously and the material re-cracked and re-healed continuously throughout the experiments. This type of behaviour is far more challenging to represent, particularly when the healing dependency on the COD and COD rate is taken into account. A new cohesive zone damage-healing model to represent this behaviour is described in Sections 3 and 4.

In the description of the model, parameters related to healed material are designated with the subscript h. The model distinguishes between the first and subsequent occurrences of damage and healing, the former being designated 'virgin' events (subscript v) and the latter with the prefix 're-' (subscript r).

2.4. Cohesive-zone crack-plane model

The cohesive-zone model uses the concept of a 'crack-plane', which is defined as the mid surface of a narrow band that contains a macro-crack and/or a number of micro-cracks (Jefferson and Mihai, 2015). The crack-plane model relates the crack-plane tractions ($\widetilde{\sigma}$) to the relative-displacements across the crack plane ($\widetilde{\mathbf{u}}$), with the three

components of both the $\widetilde{\sigma}$ and $\widetilde{\mathbf{u}}$ vectors coinciding with the directions $\mathbf{r}_1$ to $\mathbf{r}_3$ ($\mathbf{r}_1$ being normal to the crack-plane mid-surface, and $\mathbf{r}_2$ & $\mathbf{r}_3$ orthogonal in-plane directions). Prior to cracking, the relationship between $\widetilde{\sigma}$ and $\widetilde{\mathbf{u}}$ is defined by the following elastic constitutive relationship:

$$\widetilde{\sigma} = \widetilde{\mathbf{k}}^e \widetilde{\mathbf{u}}^e \tag{3}$$

where $\widetilde{\mathbf{k}}^e$ is an elastic crack-plane constitutive matrix that depends on the elastic moduli of the cementitious material (E_c) and the assumed width of the cracking zone (h_{fpz}) (Appendix A). $\widetilde{\mathbf{u}}^e$ is the elastic relative-displacement vector. The inelastic component of $\widetilde{\mathbf{u}}$ is obtained from $\widbreve{\mathbf{u}} = \widetilde{\mathbf{u}} - \widetilde{\mathbf{u}}^e = \widetilde{\mathbf{u}} - \widetilde{\mathbf{k}}^{e^{-1}}\widetilde{\sigma}$ and the COD is taken as the first component of $\widbreve{\mathbf{u}}$ i.e. $u_1\breve{}$. $u_1\breve{}$ is assumed to be equal to a normal COD measured in an experiment (i.e. $u_1\breve{} = w_c$). The components of $\widetilde{\sigma}$ are also equal to the normal and shear components of the transformed total stress tensor (i.e. $\widetilde{\sigma} = [\sigma_{1'1'}\sigma_{1'2'}\sigma_{1'3'}]^T$) with $1'$, $2'$ and $3'$ corresponding to the crack plane directions $\mathbf{r}_1, \mathbf{r}_2$ to $\mathbf{r}_3$ respectively.

This type of cohesive zone model may be applied to interface finite elements as well as to embedded discontinuities within finite elements (De Maio et al., 2021). Such models may also be applied to crack planes within finite elements using a smeared model, with the equivalent relative-displacements being computed from the transformed strains multiplied by an element characteristic length (Jefferson and Mihai, 2015).

3. Damage-healing model

Our approach to developing a damage-healing model for use in our coupled finite element program was first to select a viable theoretical framework based on our experimental observations (see Section 2.3) and then to use a discrete ligament model to explore damage-healing characteristics over a representative area of crack. The results from a series of ligament model simulations were used to guide the development of a homogenised crack-plane damage-healing model.

The ligament and homogenised damage-healing models discussed in this section are independent of the COD and assume that cracks fill instantaneously with healing agent. Here, we concentrate on understanding the damage, re-damage, healing and re-healing processes over a representative area. COD and COD rate effects are addressed using the overlapping curing front model described in Section 4, along with the method used for relating the curing front variables to the homogenised healing variables.

3.1. Damage and healing discrete ligament model

Using the ideas from statistical damage theories (Krajcinovic, 1996), we assume that virgin and healed strengths of nominal ligaments ($f_v(\xi)$ and $f_h(\xi)$ respectively) of a representative cracking-healing area (A_r) may be defined in terms of a relative area variable $\xi \in [0, 1]$. These
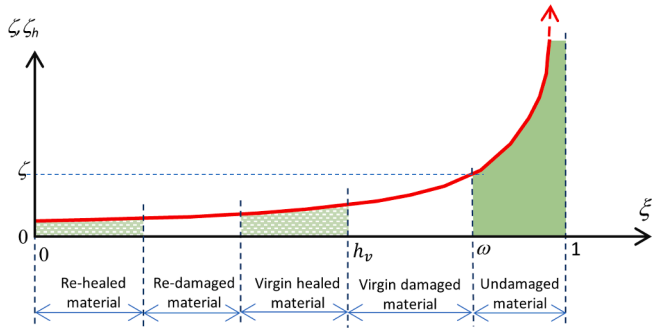
Fig. 4. Material states in terms the relative area variable (ξ), illustrated for the case in which the damage and re-damage evolution functions have the same material parameters.

strengths are arranged in order of increasing rupture strength (i.e. $f_{v,h}(\xi + d\xi) \geq f_{v,h}(\xi)$) and are related to the associated relative-displacement limits ($\zeta_\xi(\xi)$ and $\zeta_{\xi h}(\xi)$), as follows:

$$f_v(\xi) = \widetilde{k}_1^e \zeta_\xi(\xi) \text{ and } f_h(\xi) = \widetilde{k}_{h1}^e \zeta_{\xi h}(\xi) \tag{4}$$

where $\widetilde{k}_1^e$ and $\widetilde{k}_{h1}^e$ are elastic normal stiffnesses (Appendix A) for virgin and healed material respectively, and A_r is nominally assumed to be $\sim (5 d_{agg})^2$, where d_{agg} is the coarse aggregate particle size (see Gitman et al. (2007) for a discussion on representative volumes).

The proportion of damaged material is given by the damage variable $\omega(\zeta) \in [0, 1]$, where ζ is the maximum effective relative-displacement ($\zeta_{ef}(\widetilde{\mathbf{u}}, t)$) experienced by an increment of material over the time interval t_0 to t. Furthermore, the value of the relative area variable ξ for $\zeta =$

$\zeta_\xi(\xi)$ is equal to the damage variable $\omega(\zeta)$. This damage variable can be described as a cumulative probability function $P_b(\zeta)$ which gives the proportion of material that is likely to be damaged when the relative-displacement parameter is equal to ζ (Krajcinovic, 1996). The corresponding damage variable for healed material is denoted $\omega_h(\zeta_h)$ and functions for ζ_{ef}, ω and ω_h are given in Appendix A.

The link between ξ and the effective relative-displacement parameters is illustrated in Fig. 4 for a particular damage-healing scenario that involves damage, healing, re-damage and re-healing.

When an open fractured ligament heals, healing-agent fills and cures in the open space between the crack faces. This introduces a healing relative-displacement $\widetilde{\mathbf{u}}_{h\xi}(\xi, t)$ that is equal to $\widetilde{\mathbf{u}}$ at the time of healing. This means that that there is no change in stress in a ligament due to healing alone, which is important from a thermodynamic point of view (Appendix B). Taking this healing relative-displacement into account, the traction vector ($\widetilde{\sigma}_{h\xi}(\xi, t)$) on a healed material increment may be written as follows:

$$\widetilde{\sigma}_{h\xi}(\xi, t) = \widetilde{\mathbf{k}}^h \left(\widetilde{\mathbf{u}}(t) - \widetilde{\mathbf{u}}_{h\xi}(\xi, t) \right) \tag{5}$$

where $\widetilde{\mathbf{k}}^h$ is the elastic crack-plane constitutive matrix for the healed material.

Considering infinitesimal ligaments ($d\xi$) of undamaged and damage-healed material, the total traction vector by may be obtained by integrating across the representative area, as follows:

$$\widetilde{\sigma}(t) = \int_0^1 \left((1 - \mathrm{H}_\omega(\xi, t)) \widetilde{\mathbf{k}}^e \widetilde{\mathbf{u}}(t) + \mathrm{H}_\omega(\xi, t) \mathrm{H}_h(\xi, t) \widetilde{\mathbf{k}}^h \left(\widetilde{\mathbf{u}}(t) - \widetilde{\mathbf{u}}_{h\xi}(\xi, t) \right) \right) d\xi$$
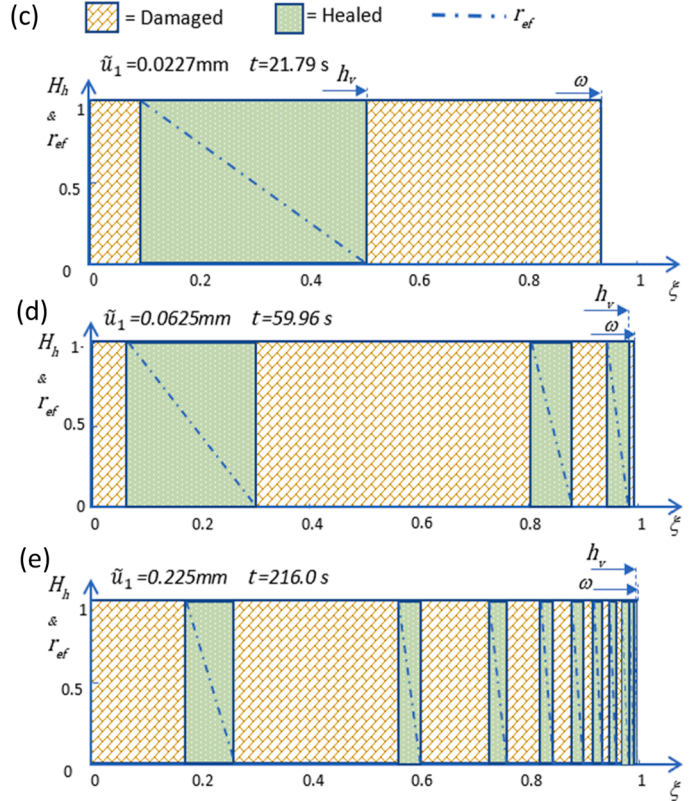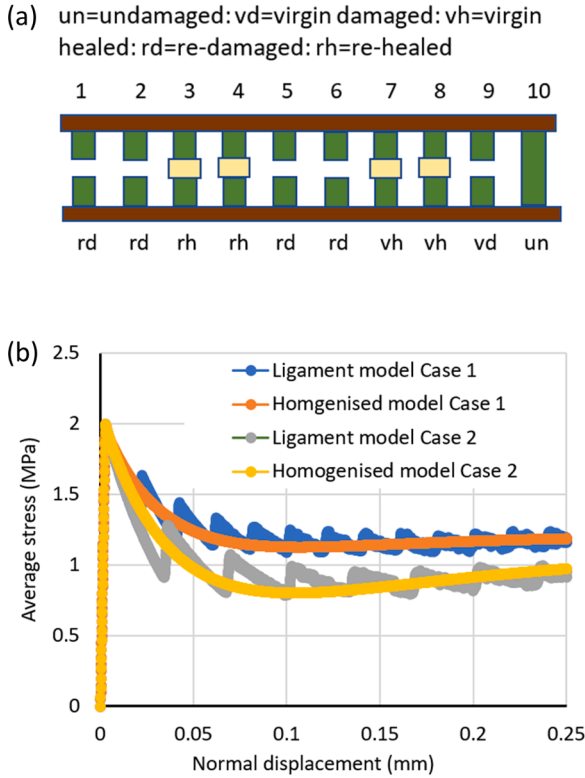
$$\tag{6}$$

Fig. 5. (a) Schematic of ligament model. (b) Comparisons of ligament and homogenised model responses for cases 1 and 2. (c)-(e) Distribution of damaged and healed material from the case 1 ligament model solution at three separate displacements.

where H_ω and H_h are Heaviside functions indicating damage and healing respectively, with $H_\omega = 0$ and $H_h = 0$ indicating undamaged and un-healed ligaments respectively, and $H_\omega = 1$ and $H_h = 1$ denoting damaged and healed ligaments respectively; noting that an infinitesimal ligament ($d\xi$) is damaged or re-damaged when $\zeta_{ef}(\widetilde{\mathbf{u}}, t)$ or $\zeta_{ef}\left(\left(\widetilde{\mathbf{u}} - \widetilde{\mathbf{u}}_{h\xi}(\xi, t)\right)\right)$ exceeds $\zeta_\xi(\xi)$ or $\zeta_{\xi h}(\xi)$ respectively. Furthermore, H_h changing from 1 to 0 signifies a re-damage event.

If $\widetilde{\mathbf{u}}$ changes with time during the healing process, the stress and crack-healing displacement will vary across A_r. To explore this situation, the traction history across A_r has been evaluated over a time interval t_0 to t_n at n_t discrete times (t_i) using the following discrete approximation of (6):

$$\widetilde{\sigma}(t_i) = \sum_{j=1}^{n_l} \widetilde{\sigma}_{\xi_j} \Delta\xi = \sum_{j=1}^{n_l}\left[\left(1 - H_{\omega_j}\right)\widetilde{\mathbf{k}}^{\mathrm{e}}\widetilde{\mathbf{u}}_j + H_{\omega_j}H_{h_j}\widetilde{\mathbf{k}}^{\mathrm{h}}\left(\widetilde{\mathbf{u}}_j - \widetilde{\mathbf{u}}_{h\xi_j}\right)\right]\Delta\xi \tag{7}$$

where n_l is the number of discrete ligaments, $\Delta\xi = 1/n_l$, subscript j denotes the value of a variable at $\xi = \xi_j$ and $\Delta t = (t_n - t_0)/(n_t - 1)$; the time subscript i has been dropped from the right-hand-side terms for clarity.

The scenario chosen to illustrate the features of the damage-healing process is a band of cementitious material with the geometric and ma-terial properties given in Table A1 (Appendix A). A schematic of the system with 10 ligaments is shown in Fig. 5a. A normal displacement ($\widetilde{u}_1$) is applied to all ligaments at a constant rate, from time 0 to t_{max}, until it reaches the maximum value u_{lim}. This creates a state of uniaxial tension in the band and so only scalar stress and relative-displacement measures are considered. It is assumed that there is a fixed time inter-val (Δt_h) between a ligament fracturing and re-healing (Table A1). Two cases are considered, which have the following maximum displacement and duration: case 1 $u_{lim} = 0.25$ mm and $t_{max} = 240$ s: and case (ii) $u_{lim} = 0.25$ mm and $t_{max} = 60$ s.

The overall traction-relative-displacement response of the system is given for both cases in Fig. 5b. The proportions of material that are damaged and healed at three selected times for case 1 are shown in Fig. 5c–e. This figure also shows the value of a parameter $r_{ef}(\xi, t) = \left(\zeta_{ef}\left(\left(\widetilde{\mathbf{u}} - \widetilde{\mathbf{u}}_{h\xi}\right), t\right)\middle/\zeta_{h\xi}\right)$, which provides a measure of how close a material increment is to the re-damage surface. $r_{ef} = 1$ indicates material that is on the re-damage surface and $r_{ef} = 0$ is associated with unstressed material. A convergence study showed that $n_l = n_t = 4000$ gave trac-tions results that were converged to within 1%, which was considered adequate for the present purposes.

The behavioural characteristics exhibited by the ligament model in this solution, in ξ space, include;

I. the healing front (h_v) progresses from $\xi = 0$ towards $\xi = 1$, with damaged material becoming interspersed with healed material in the range 0 to h_v as the applied displacement increases;
II. it appears that discrete blocks of healed material (resembling waves) form within the range 0 to h_v, and the number and size of these blocks tend to increase and decrease respectively as the damage-healing process proceeds; although the blocks would not necessarily manifest in this way in reality, since they artefacts of the increasing-strength representation in ξ space;
III. $\widetilde{\mathbf{u}}_{h\xi}$ may vary in the range 0 to h_v in an irregular manner;
IV. r_{ef} may vary from 0 to 1 within a block of healed material, implying a considerable variation in the propensity of different ligaments to re-damage with further displacement.

3.2. Damage and healing homogenised model

The above characteristics, along with some experimental observa-tions and theoretical considerations, led to a set of assumptions on which the homogenised model is based. These assumptions, the relevant characteristics determined from the discrete model (I-IV) and associated model components are now considered.

(i) *Assumption:* a homogenised form of Eq. (6) exists that relates the averaged traction vector to the relative-displacement vector, and which depends on the scalar damage variable (ω) and a healing variable ($h \in [0, \omega]$), as well as a homogenised healing relative-displacement vector $\widetilde{\mathbf{u}}_h$, as follows:

$$\widetilde{\sigma}(t) = (1 - \omega(t))\widetilde{\mathbf{k}}^{\mathrm{e}}\widetilde{\mathbf{u}}(t) + h(t)\widetilde{\mathbf{k}}^{\mathrm{h}}\left(\widetilde{\mathbf{u}}(t) - \widetilde{\mathbf{u}}_h(t)\right) \tag{8}$$

(ii) Characteristics I and II from the discrete model solution (Section 3.1) suggest that the re-damaged material should be expressed as a proportion of h_v and that this may be related to the homoge-nised healing variable as follows:

$$h = (1 - \omega_h(\zeta_h))h_v \tag{9}$$

where ζ_h is the homogenised effective healed relative-displacement.

Remark: The total amount of material that is re-damaged at any one time can grow and diminish, which implies that ω_h is not a conventional irreversible damage variable since it reduces when re-healing occurs.

(iii) *Assumption*: a time-dependent healing function exists that gives the proportion of material that is healed at time t in the absence of any re-damage. The following exponential healing function, used by other investigators (Mergheim and Steinmann, 2013), is assumed for the purpose of comparing the responses computed from the homogenised and ligament models:

$$h_f(t, t_{co}) = 1 - e^{-\langle t - t_{co}\rangle/\tau_h} \tag{10}$$

where $\langle x \rangle$ denotes Macauley brackets such that $\langle x \rangle = x$ if $x \geq 0$ and $= 0$ if $x < 0$, t_{co} is the time when curing begins and τ_h is the healing time parameter.

Remarks: a linear homogenised healing model may be more consis-tent with the fixed healing period used in the ligament model; however, the linear function is far less convenient than (10) because of the need to track the end of the healing period after each occurrence of re-damage. Also, it was found that the response from the linear model in the range $t = 0$ to τ_h (before the tracking is required) was very similar to that ob-tained with (10) for the parameter ranges considered. A more accurate approach for computing healing, which accounts for COD and COD rate dependency, is presented in Section 4.

(iv) The healing variable may be derived from the following convo-lution integral (Mergheim and Steinmann, 2013):

$$h(t) = \int_0^t h_f(t, s)\frac{\partial a(s)}{\partial s}ds \tag{11}$$

where $a(s)$ represents the relative area of curing healing-agent within the crack at time s.

Remarks: h and a change when re-damage occurs. (11) also applies to h_v but this variable does not reduce with re-damage.

(v) Characteristic III (Section 3.1) relates to the variation of $\widetilde{\mathbf{u}}_{h\xi}(\xi, t)$ in the ξ range (0 to h_v). A homogenised healing displacement vector ($\widetilde{\mathbf{u}}_h$) may be derived from (6), for a particular time t, as follows:

$$\widetilde{\mathbf{u}}_h = \frac{1}{h}\int_0^{h_v} \mathrm{H}_\omega(\xi)\mathrm{H}_h(\xi)\widetilde{\mathbf{u}}_{h\xi}(\xi)\mathrm{d}\xi \tag{12}$$

This expression is not convenient for the homogenised model since $\widetilde{\mathbf{u}}_{h\xi}(\xi, t)$ is not available. We therefore use the condition that a positive healing rate and zero damage rate should result in a zero stress rate. This condition ensures that no spurious strain energy is created when healing occurs (Appendix B) and may be expressed by the following rate equation:

$$\left(\left(h + \dot{h}\right)\widetilde{\mathbf{k}}^h\left(\widetilde{\mathbf{u}} - \widetilde{\mathbf{u}}_h - \dot{\widetilde{\mathbf{u}}}_h\right)\right) - h\widetilde{\mathbf{k}}^h\left(\widetilde{\mathbf{u}} - \widetilde{\mathbf{u}}_h\right) = 0 \tag{13}$$

where the superior dot denotes a time derivative.

An equation for the $\widetilde{\mathbf{u}}_h$ rate may be derived from (13) by neglecting second order terms, as follows:

$$\dot{\widetilde{\mathbf{u}}}_h = \frac{\dot{h}\left(\widetilde{\mathbf{u}} - \widetilde{\mathbf{u}}_h\right)}{h} \tag{14}$$

and in the absence of re-damage, $\widetilde{\mathbf{u}}_h = \int_{t_0}^t \dot{\widetilde{\mathbf{u}}}_h \mathrm{d}t$.

Remark: an equivalent expression may be derived for $\widetilde{\mathbf{u}}_h$ by considering the contribution of each infinitesimal healing increment to its value (i.e. $\mathrm{d}\,\widetilde{\mathbf{u}}_h = \left(\dot{h}\widetilde{u}(t)/h\right)\mathrm{d}t$). This results in a convolution integral for $\widetilde{\mathbf{u}}_h$, which is used for proving the thermodynamic validity of the model (Appendix B).

(vi) Characteristic IV (Section 3.1) relates to the variation of r_{ef} across ξ and the implied variation of $\zeta_{h\xi}$. As with $\widetilde{\mathbf{u}}_h$, it is inconvenient to derive ζ_h from an integral expression involving an approximation of $\zeta_{h\xi}$ across ξ. A more convenient, and consistent, approach is to derive a homogenised value for ζ_h using the following condition:

Solve $h - (1 - \omega_h(\zeta_h))h_v = 0$ for ζ_h $\tag{15}$

(vii) *Assumption:* healing-agent is supplied instantaneously to damaged or re-damaged material increments, which implies that all of the damaged material is undergoing curing i.e. $a = \omega$.

Remark: this assumption is not made in the coupled model described in Section 4, in which crack filling is simulated explicitly.

(viii) *Assumption:* h reduces when re-damage occurs at the rate $\dot{h} = -\dot{\omega}_h h_v$.

In order to compare the response of the homogenised model (8) with that of the discrete model (7), an algorithm is needed to integrate (8) over a specified relative-displacement path for the same time period considered for the ligament model (Fig. 5). The algorithm employs the following standard recursive relationship for updating the healing variables, which is based on the convolution integral (11) (Simo and Hughes, 1998; Mergheim and Steinmann, 2013):

$$h_i = h_{i-1}e^{-\Delta t/\tau_h} + a_i\left(1 - e^{-\Delta t/\tau_h}\right) \tag{16}$$

$$h_{v_i} = h_{v_{i-1}}e^{-\Delta t/\tau_h} + a_i\left(1 - e^{-\Delta t/\tau_h}\right) \tag{17}$$

where the value of a variable at time t_i is denoted with subscript i.

It is assumed that, within a time increment, damage and healing may be computed sequentially, provided that the time-step is converged. We assume that a response is time-step converged when the response at any time does not change by more than 0.1% when the time-step is halved.

In the damage sub-step, ω and ω_h may increase, whilst h_v remains constant and h reduces in accordance with (9), with the adjusted value being denoted h_p. In the healing sub-step, h and h_v are updated, and ζ_h

and the dependent ω_h are computed using (16) and (17).

The algorithm is presented in algorithm Box 1.

Algorithm 1. Homogenised crack-plane damage-healing model algorithm for comparison with ligament model

---

$t = t_0$ Initialise ζ_0, ζ_{h0}, h_{v_0} and $\widetilde{\mathbf{u}}_{h_0}$
for $i = 1$ to n_{step}
   $t_i = t_{i-1} + \Delta t$
   $\widetilde{\mathbf{u}}_i = \widetilde{\mathbf{u}}(t_i)$
   Damage sub-step
      $\zeta_i = \max(\zeta_{i-1}, \zeta_{ef}(\widetilde{\mathbf{u}}_i))$ and $\zeta_{h_i} = \max(\zeta_{h_{i-1}}, \zeta_{ef}(\widetilde{\mathbf{u}}_i - \widetilde{\mathbf{u}}_{h_i}))$
      $h_p = \left(1 - \omega_h(\zeta_{h_i})\right)h_{v_{i-1}}$
   Healing sub-step
      $a_i = \omega(\zeta_i)$
      $h_i = h_p e^{-\Delta t/\tau} + a_i\left(1 - e^{-\Delta t/\tau_h}\right)$
      $h_{v_i} = h_{v_{i-1}}e^{-\Delta t/\tau} + a_i\left(1 - e^{-\Delta t/\tau_h}\right)$
      $\widetilde{\mathbf{u}}_{h_i} = \widetilde{\mathbf{u}}_{h_{i-1}} + \dfrac{(h_i - h_p)\left(\widetilde{\mathbf{u}} - \widetilde{\mathbf{u}}_h\right)}{h_i}$
      Solve $h_i - \left(1 - \omega_h(\zeta_{h_i})\right)h_{v_i} = 0$ for ζ_{h_i}
      $\widetilde{\sigma}_i = (1 - \omega_i)\widetilde{\mathbf{k}}^e\widetilde{\mathbf{u}}_i + h_i\widetilde{\mathbf{k}}^h\left(\widetilde{\mathbf{u}}_i - \widetilde{\mathbf{u}}_{h_i}\right)$
End for loop

Note: $\max(a,b) =$ larger of a or b.

3.3. Comparison between discrete and homogenised models

A comparison between the predicted responses from the ligament and homogenised models for cases 1 and 2 is shown in Fig. 5b. In both cases, the response of the homogenised model lies within the response envelope of the discrete model, which provides an indication that the assumptions used in to derive the homogenised model are reasonable. Matching the response of the ligament model is not an end within itself. The final arbiter of the accuracy of the model lies in its ability to reproduce a good range of experimental responses. Before these are considered in Section 6, the issue of the healing dependency on the COD and its rate is addressed.

4. The computation of healing from interacting curing fronts

As illustrated in Fig. 2, the degree of cure in an open crack varies across the body of healing-agent. Measurable mechanical healing commences when a solid phase of material first percolates across the body of healing-agent. This occurs after the symmetrical curing fronts from opposing crack surfaces overlap, with the degree of cure at the centre of the crack being $2\phi_m$, where $\phi_m = \phi(w_c/2, z_f)$. If the degree of healing were determined using a classical Evans-Avrami phase-change model (Wool and O'Connor, 1981), $h_f = 1 - e^{-2\phi_m}$; however, this function did not accurately represent the behaviour of our direct tension tests, as illustrated in Section 6. Rather, we found that once a threshold had been reached, the degree of healing is well-approximated using the assumption that the degree of healing is equal to ϕ_m. Setting $x = 0.5w_c$ gives the following expression for the degree of healing in a stationary crack (h_{f_stat}):

$$h_{f\_stat}\left(w_c, z_f\right) = \phi_m = \frac{1}{2}\left(1 - tanh\left(\frac{0.5w_c - z_f - z_{c2}}{z_{c2} + \sqrt{z_f/z_{c1}}}\right)\right) \tag{18}$$

Eq. (18) represents the degree of healing when the COD rate is zero throughout the healing period; however, when the COD changes, two important changes are required to capture COD rate effects. The first is to introduce a term $(\Theta\left(\dot{w}_c\right))$ that accounts for the disruption in the propagation of the polymerisation reaction caused by significant movement in the body of healing-agent. The second is to replace z_f by a generalised curing front variable $\bar{z}$ that is accumulated in the manner described below.

Table 2
Summary of damage, healing and curing front variables.

Variable	Description	Calculated from
ω	Virgin damage variable that depends on the ζ	$\zeta = \max(\zeta_{prev}, \zeta_{ef}(\widetilde{\mathbf{u}}))$
ω_h	Re-damage variable that depends on ζ_h	At damage sub-step: $\zeta_h = \max(\zeta_{h_{prev}}, \zeta_{ef}(\widetilde{\mathbf{u}}_i - \widetilde{\mathbf{u}}_{h_i}))$ At healing sub-step: ζ_h is computed from $h - (1 - \omega_h(\zeta_h))h_v = 0$
$\overline{z}$	Generalised curing front variable	Accumulated during a healing sub-step according to Eq. (29)
$\overline{z}_v$	Generalised virgin curing front variable	Accumulated during a healing sub-step according to (24)
$\overline{z}_r$	Generalised curing front variable adjusted for re-damage	Calculated at the end of a damage sub-step according to (28)
h_v	Virgin healing variable	Accumulated in increments computed from previous and current values of $\overline{z}_v$ using (30)
h	Current healing variable	After damage sub-step: $h = (1 - \omega_h(\zeta_h))h_{v_{prev}}$ During the healing sub-step: h is computed from (31), using $\overline{z}_r$ and incremental healing changes resulting from changes in $\overline{z}$
$\widetilde{\mathbf{u}}_h$	Healing relative-displacement	Updated during the healing sub-step using an incremental form of (14) i.e. $\widetilde{\mathbf{u}}_{h_i} = \widetilde{\mathbf{u}}_i\left(1 - \dfrac{h_r}{h_i}\right) + \widetilde{\mathbf{u}}_{h_{i-1}}$ Fixed during the damage sub-step.

By considering the $\dot{w}_c$ rates in all of the tests (Selvarajoo et al., 2020a), we found that $\Theta\left(\dot{w}_c\right)$ was unity for nominally static cracks (i.e. $\dot{w}_c$ was less than the threshold rate (w_{rt})) but approximately half this value when the rate exceeded the threshold. In the absence of detailed data around the threshold, we propose the following function that provides a smooth transition between the nominally static and dynamic crack rate domains:

$$\Theta\left(\dot{w}_c\right) = \left(\frac{f_{stat} + f_{dyn}}{2}\right) - \left(\frac{f_{stat} - f_{dyn}}{2}\right)\tanh\left(\frac{\dot{w}_c - w_{rt}}{w_{rnom}}\right) \tag{19}$$

where the static and dynamic factors are $f_{stat} = 1$ and $f_{dyn} = 0.45$ respectively, $w_{rt} = 10^{-3}\zeta_m/\tau_h mm/s$ and $w_{rnom} = w_{rt}/10$.

Eq. (18) is then replaced by the function that gives an equivalent degree healing for a given value of $\overline{z}$:

$$h_f(w_c, \overline{z}) = \frac{\Theta\left(\dot{w}_c\right)}{2}\left(1 - tanh\left(\frac{0.5w_c - \overline{z} - z_{c2}}{z_{c2} + \sqrt{\overline{z}/z_{c1}}}\right)\right) \tag{20}$$

The generalised front variable is described into terms of the following convolution integral:

$$\overline{z} = \int_0^{t_c} z_{c0}\left(1 - e^{-(t_c - s)/\tau}\right)\frac{\partial a(s)}{\partial s}ds \tag{21}$$

where $a(t_c) = A_c(t_c)/A_{cg}$ is the relative area of a crack at a crack integration point that is undergoing curing, with A_c being the actual area undergoing curing and A_{cg} being the area associated with a crack numerical integration point or, in a general context, a representative crack area.

$a(t_c)$ depends on the curing time, the level of damage (ω) and the proportion of area filled with healing-agent (r_{fill}). Defining the relative fill area ($a_{fill} = \omega r_{fill}$) and making the assumption that an incremental component of healing-agent starts to cure immediately it is exposed to a new surface of crack wall, a accumulates as follows:

$$a = \int_{t_0}^t \dot{a}_{fill}dt \tag{22}$$

As with (11), the convolution integral (21) may be solved over a finite time interval using the following recursive expression:

$$\overline{z}_i = \overline{z}_{i-1}e^{-\Delta t/\tau} + z_{c0}a_i\left(1 - e^{-\Delta t/\tau}\right) \tag{23}$$

The virgin generalised curing front variable $\overline{z}_v$, given in Eq. (24), is also required and this is used to compute the virgin healing front variable (h_v).

$$\overline{z}_{v_i} = \overline{z}_{v_{i-1}}e^{-\Delta t/\tau} + z_{c0}a_{v_i}\left(1 - e^{-\Delta t/\tau}\right) \tag{24}$$

An increment of healing (Δh) is then computed using (20), as follows:

$$\Delta h = h_f(w_{c_i}, z_i) - h_f(w_{c_{i-1}}, z_{i-1}) \tag{25}$$

and,

$$h_i = h_{i-1} + \Delta h \tag{26}$$

where h_i now represents the accumulated degree of healing at time t_i.

(20) to (26) allow healing to be simulated for a crack with a time-varying fill-area, but further consideration is required to allow for re-cracking and re-healing. When re-cracking occurs, the accumulated curing front and healing variables must be reduced due to the loss of area (a_{red}). This is achieved by first reducing h by a_{red} to give h_r, as shown in (27), and then equating (20) to h_r to find the consistent value of $\overline{z}$ (denoted z_r), as shown in (28), in which $c_h = \text{atanh}(2\frac{h_r}{\Theta(w_c)} - 1)$.

$$h_r = h_{i-1} - a_{red} \tag{27}$$

$$z_r = z_{fw}(h_r, w_c) = \frac{\left[c_h + \sqrt{c_h{}^2 + 2z_{c1}\left(2z_{c2}(c_h - 1) + w_c\right)}\right]^2}{4z_{c1}} \tag{28}$$

This results in (23) being replaced with Eq. (29), as follows:

$$\overline{z}_i = \overline{z}_r e^{-\Delta t/\tau} + z_{c0}a_i\left(1 - e^{-\Delta t/\tau}\right) \tag{29}$$

Furthermore, it is necessary to account for the healed material present in the crack when re-damage and re-healing occur. This is accomplished by introducing the re-crack opening displacement ($w_r = w_c - w_h$) into the healing update (25), as calculated from the current total crack and healed crack displacements.

The accumulated virgin healing variable (h_v) and the current healing variable are then computed using the following expressions:

$$h_{v_i} = h_{v_{i-1}} + \Delta h_v \tag{30}$$

$$h_j = h_r + \Delta h_{rh} + \Delta h_v \tag{31}$$

where Δh_v and Δh_{rh} are the virgin and re-healing increments respectively.

These steps form the basis of the damage-healing algorithm presented in Section 5.2.

The consistent set of damage, curing front and healing variables described in Sections 3 and 4 are summarised in Table 2.

5. Computational framework and solution algorithm

5.1. Overall solution framework

We use the finite element method to solve the nonlinear coupled transport solid-mechanics problem using a staggered solution method. The governing equations for discrete and continuum healing-agent flow are given in Appendix C, and we use a conventional virtual work approach to derive the governing solid-mechanics system of equations. The discretised form of these equations is derived in the standard manner (Zienkiewicz et al., 2014) and may be expressed by the

Table 3

Mechanical material parameters used for the analyses.

Example	E, E_h kN/mm^2	ν, ν_h	f_t N/mm^2	f_{th} N/mm^2	ζ_m mm	ζ_{hm} mm	τ s	z_{c0} mm	z_{c1} mm	w_{c_th} mm
1	30	0.2	3.5	3.4	0.2	0.2	60	0.1	25	0.05
2	30	0.2	2.9	3.4	0.15	0.09	60	0.1	25	0.05
3	30	0.2	2.5	3.4	0.18	0.09	60	0.1	25	0.02

ν = Poisson's ratio.

following matrix equation for the nonlinear system:

$$\mathbf{K}_g\big(\mathbf{u}_g\big)\mathbf{u}_g = \mathbf{F}_g \tag{32}$$

where $\mathbf{u}_g$ is the global nodal displacement vector, $\mathbf{K}_g(\mathbf{u}_g)$ is the global nonlinear stiffness matrix and $\mathbf{F}_g$ is the global vector of nodal loads.

$\mathbf{K}_g(\mathbf{u}_g)$ is assembled from the individual element stiffness matrices, which take either the standard form ($\mathbf{K}_e$), for linear uncracked elements, or the special form with an embedded strong-discontinuity ($\mathbf{K}_{sd}$) for cracked elements (Freeman et al., 2020). The nonlinear system of equations is solved using a standard Newton incremental iterative scheme (De Borst et al., 2012). This involves the nodal forces being applied in a set of time steps and then, at each time step, the out of balance force vector ($\mathbf{\Psi}$) (33) being reduced in a series of iterations to a specified tolerance as measured by an L2 norm of $\mathbf{\Psi}$.

$$\mathbf{\Psi}(t) = \boldsymbol{F}_\lambda(t) - \sum_{Ass} \int_{\Omega_e} \boldsymbol{B}^{\mathrm{T}} \boldsymbol{\sigma}_e(t)\, d\Omega_e = 0 \tag{33}$$

where $\boldsymbol{F}_\lambda(t)$ is the global applied force vector at time t, $\sum_{ASS}$ denotes the element assembly process and $\mathbf{B}$ is the strain–displacement matrix.

The solution scheme for the coupled problem is given in Algorithm box 2, in which a sequential coupling procedure is employed that utilises sub-stepping for the transport problem (Freeman and Jefferson, 2020).

Algorithm 2. Staggered solution algorithm for transport and solid-mechanics equation systems, showing damage and healing phases

$t = t_0; \mathbf{F}_\lambda(t_0) = 0$	Initialise all cumulative variables.
for $i = 1$ to n_{step}	Loop time steps.
$t_i = t_{i-1} + \Delta t$; Read $\mathbf{F}_\lambda(t_i)$	Set time variable and current loads.
Extract χ_e & w_{ce} from previous stage 2 computations	Extract crack path & widths from cracked elements.
Transport computations. Stage 1	**Stage 1:** Solve coupled discrete-continuum transport problem.
Solve for χ_{m_i} & P_{h_i}	Solve the nonlinear transport equations (Appendix C), using sub steps if necessary.
Mechanical computations. Stage 2, Phase 1. Damage	**Stage 2:** Solve the mechanical equation system (32).
	Mech Phase 1: Equilibrium and damage computations.
$\mathbf{\Psi} = \mathbf{F}_\lambda(t_i) - \mathbf{F}_\lambda(t_{i-1})$	Set out-of-balance force vector to current load increment.
for $it = 1$ to nt	Enter iteration loop.
$\delta\mathbf{u}_g = \left[\dfrac{\partial\mathbf{\Psi}}{\partial\mathbf{u}_g}\right]^{-1}(-\mathbf{\Psi})$	Solve for incremental displacements
$\mathbf{u}_g = \mathbf{u}_g + \delta\mathbf{u}_g$; compute ζ_i, ζ_{hi}, $\boldsymbol{\sigma}_j$	Update displacements, damage variables & stresses
$\mathbf{\Psi} = \mathbf{F}_\lambda(t_i) - \sum_v \int_{\Omega_e} \boldsymbol{B}^{\mathrm{T}}\boldsymbol{\sigma}_e(t_i)$	Compute out of balance forces
Exit it loop when L2($\mathbf{\Psi}$)/$\Psi_{ref} \leqslant tol$	Exit iteration loop if converged
Mechanical calculations. Stage 2, Phase 2: Healing See Algorithm 3 (Section 3.2) for update of $r_{fill_i}, a_{red}, a_{rec_i}, a_{fill_i} a_i, z_i, z_{v_i}, h_{r_i}, h_{v_i}, h_i, \widetilde{u}_{h_i}$	Compute fill, curing front and healing variables (Section 4)
End for i	End time step loop

where $\Psi_{ref} = |\boldsymbol{F}_\lambda(t_i)|$ and χ_e & χ_m denote the convected coordinate of the healing agent meniscus in a discrete crack within an element and with reference to the supply channel respectively.

5.2. Healing update algorithm

The algorithm for updating the healing variables for the damage-healing model described in Sections 3 and 4 is presented in Algorithm Box 3.

Algorithm 3. Healing variable update

Stage 2, Phase 2: Healing: time t_i

$\Delta a = \Delta \omega r_{fill} + a_{i-1}\Delta r_{fill}$: $a_{red} = \omega_{h_i} h_{v_{i-1}}$: $a_{rec} = a_{red} r_{fill}$: $a_{v_i} = a_{v_{i-1}} + \Delta a$

$a_{cr} = a_{v_i} - a_{red}$: $a_i = a_{cr} + a_{rec}$: $h_r = h_{v_{i-1}} - a_{red}$: $w_r = w_{c_i} - w_{h_{i-1}}$: $z_r = z_{fw}(h_r, w_r)$

$\overline{z}_{cr} = \overline{z}_r e^{-\Delta t/\tau} + z_{c0} a_{cr}(1 - e^{-\Delta t/\tau})$: $\overline{z}_{v_i} = \overline{z}_{v_{i-1}} e^{-\Delta t/\tau} + z_{c0} a_{v_i}(1 - e^{-\Delta t/\tau})$: $\overline{z}_i = \overline{z}_r e^{-\Delta t/\tau} + z_{c0} a_i(1 - e^{-\Delta t/\tau})$

$\Delta h_v = (h_f(w_{c_i}, \overline{z}_{v_i}) - h_f(w_{c_{i-1}}, \overline{z}_{v_{i-1}}))$: $\Delta h = \Delta h_v + (h_f(w_r, \overline{z}_{cr}) - h_f(w_r, \overline{z}_r))$: $h_{v_i} = h_{v_{i-1}} + \Delta h_v$: $h_i = h_r + \Delta h$

Solve $h_i - (1 - \omega_h(\zeta_{h_i}))h_{v_i} = 0$ for ζ_{h_i}

$\widetilde{\mathbf{u}}_{h_i} = \widetilde{\mathbf{u}}_i\left(1 - \dfrac{h_r}{h_i}\right) + \widetilde{\mathbf{u}}_{h_{i-1}}$

6. Examples and the influence of healing material parameters

We assess the predictive performance of the coupled model using test data from our own experiments (examples 1 and 2) (Selvarajoo et al., 2020a), as well as data from a well-known concrete fracture test (example 3). The latter (Nooru-Mohamed, 1992) is re-imagined as a healing test in order to explore the healing response in a specimen with a more complex crack pattern than those that occur in examples 1 and 2.

The experiments considered in examples 1 and 2 all used the same healing-agent (PC20) and design concrete mix, although it was found that there were natural variations in the concrete properties between batches. The mechanical material properties are given in Table 3 and the flow properties, which were kept the same for all of the analyses, are given in Appendix C.

The results reported in example 1 were obtained using the crack-plane model alone and this example concentrates on basic damage-healing behaviour for different CODs and healing periods. The example also considers the sensitivity of the predicted responses to variations in the healing material parameters. The analyses reported in examples 2 and 3 were undertaken using the coupled finite element program developed for this work. All of the finite element analyses were two-dimensional and employed 4-noded bilinear isoparametric elements. The staggered incremental iterative Newton solution (Algorithm 2) was used to solve the nonlinear coupled transport–mechanical equations and a convergence tolerance of 10^{-5} was used for L2 norms of the mass balance and residual force vectors. The number of time steps used for each analysis is given with each example and in every case a check was undertaken to ensure that the solutions were converged with respect to the time step size, using a tolerance 1% (based on changes in CMOD, reactions and meniscus flow position).

6.1. Example 1. Direct tension tests with different crack openings and healing periods

The direct tension (DT) experiments considered in this example used the doubly notched concrete cuboid specimens shown in Fig. 1b. In each test, the specimens were loaded until a crack opened to a pre-selected crack mouth opening displacement (CMOD) value (i.e. 0.1 mm for DT1 and 0.2 mm for DT2). The test was then paused for a specified 'healing period' (t_f) whilst healing-agent was fed into the crack via a set
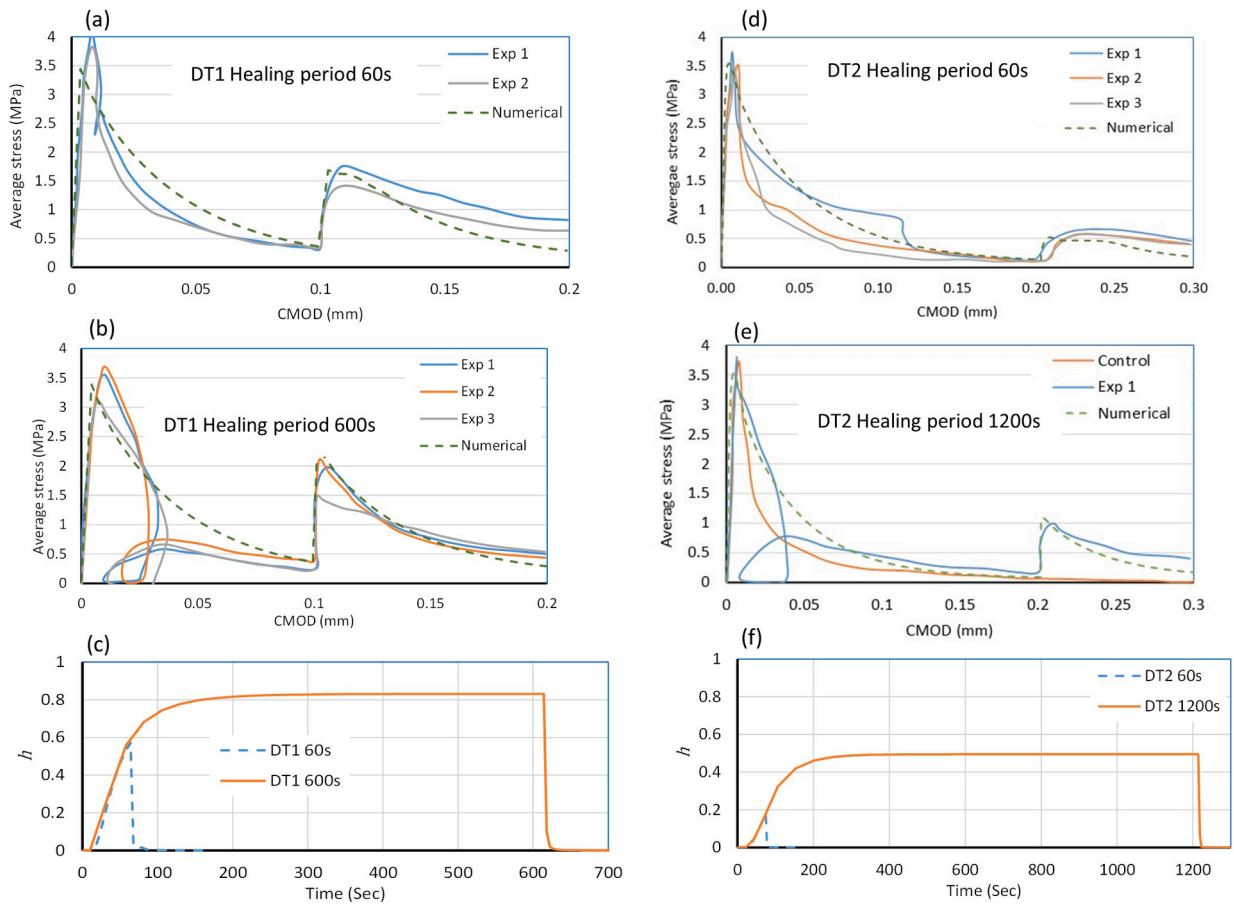
Fig. 6. Experimental and numerical responses for direct tension specimens for DT1 (a–c) and DT2 (d–f).
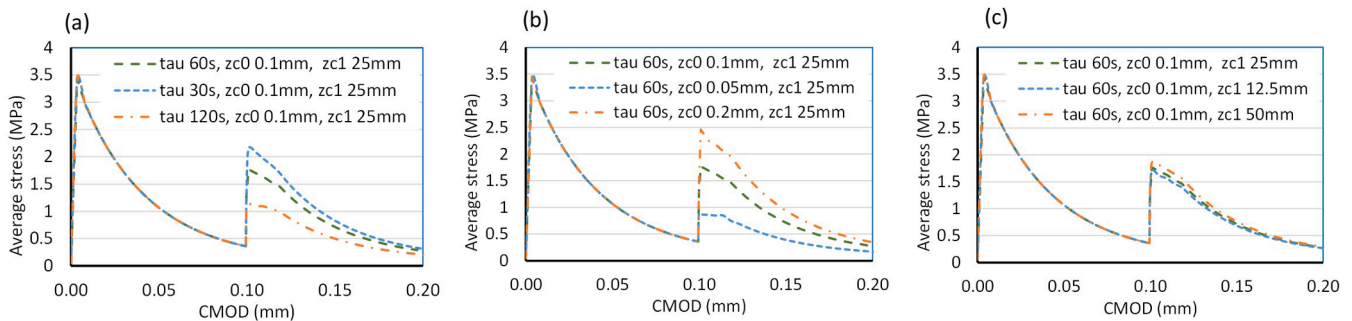

Fig. 7. Parametric study using DT1_60s data, considering variations in (a)τ, (b)z_{c0} and (c)z_{c1}.

of supply tubes and healing took place. Once the healing period had elapsed, the healing-agent supply was stopped and loading recommenced until a designated CMOD value had been attained. Here, we consider DT1 specimens with healing periods of 60 s and 600 s, and DT2 specimens with healing periods of 60 s and 1200 s.

In the experiments it was observed that the healing-agent did not cure over the full crack area, and to account for this we have used an effective curing area of 70% and 60% of the unnotched ligament for the DT1 and DT2 analyses respectively. For all but the final set (DT2_1200 secs), three tests were conducted with the same test parameters, in addition to a no-healing control test. Results from an example control test are included in the DT2_1200s graph. We have removed the results from those tests with known experimental problems (Selvarajoo et al., 2020a). A relevant experimental observation was that uncured healing-agent was present in the crack after the supply was stopped for both of

the 60 s healing period tests. This was simulated by assuming that the supply continued for 20 s after the supply tubes were clamped. This time corresponds approximately to when the outflow of healing-agent from the exit tubes was observed to cease.

In some of the experiments, the response in the first phase of loading exhibited an unloading–reloading loop (see Fig. 6b). This, along with other characteristics of the pre-healed softening response, are discussed in Selvarajoo et al. (2020a). The form of the cohesive-zone model presented in this paper does not account for this type of non-linear unloading–reloading response, but it would be possible to enhance the model to include such behaviour using an approach developed by the first author (Jefferson, 2002: Jefferson and Mihai 2015).

A comparison between the experimental and numerical responses is given in Fig. 6 along with predicted healing time-histories. The average stress in the graphs is defined as the applied load divided by the
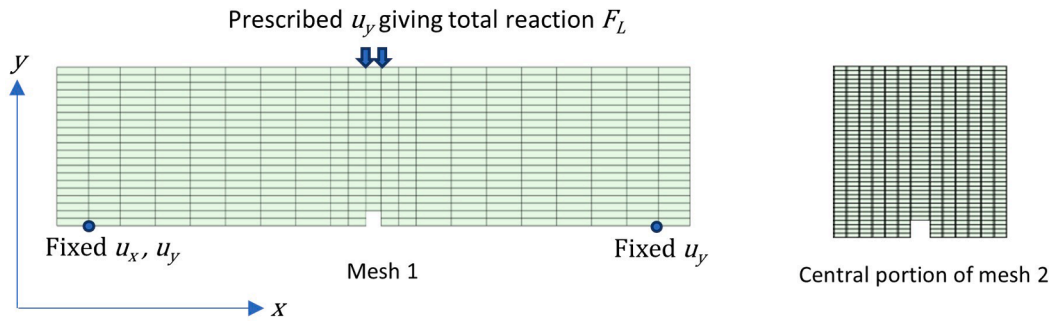
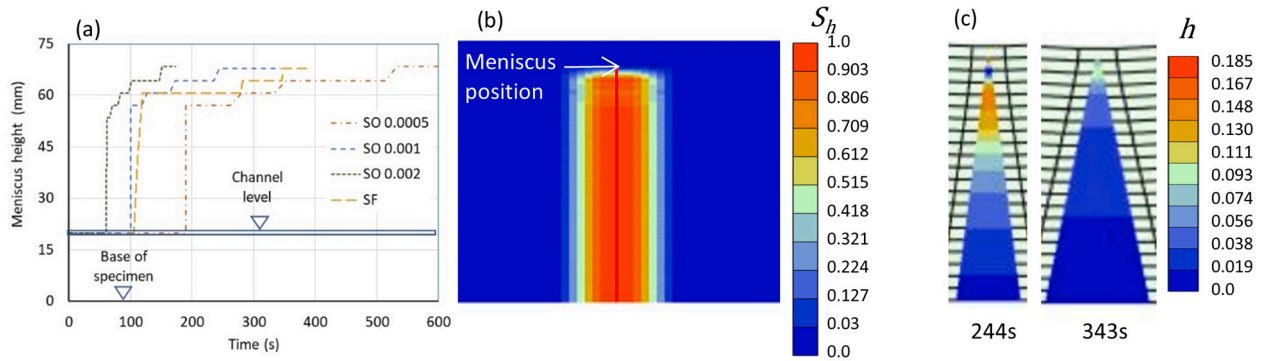**Fig. 8.** Finite element meshes used for example 2.

Fig. 9. (a) Meniscus rise responses from SO and SF analyses. (b) Meniscus position and degree of saturation at $t = 343$ s for SO_0.001. (c) Degree of healing in crack at $t = 244$ s and 343 s for SO_0.001.
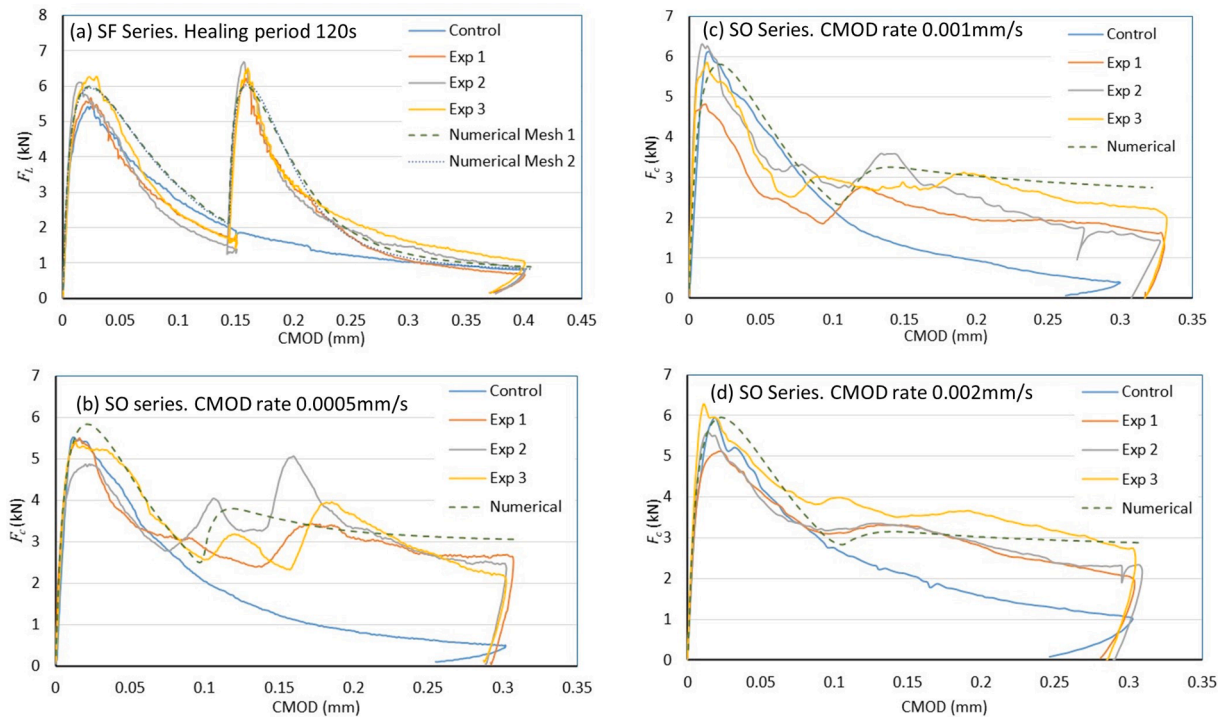

Fig. 10. Experimental and numerical responses for (a) fixed healing period test (SF), and (b)-(d) variable crack opening tests at different CMOD rates (SO).

unnotched area (i.e. $F_L/5000$ N/mm²). Fig. 6 shows that the model is able to reproduce the major experimental trends with good accuracy; namely, (i) less healing occurs in a 0.2 mm crack than the 0.1 mm crack, and (ii) the tests with 60 s healing periods exhibit less healing than those with a t_f of 600 s and 1200 s for DT1 and DT2 respectively. The

numerical responses beyond the healing peak load are apparently less ductile than the experimental responses, particularly in the 60 s healing-period cases. These differences are attributed to a flux in the uncured healing-agent beyond the end of the effective supply time that was not simulated in these crack-plane analyses.
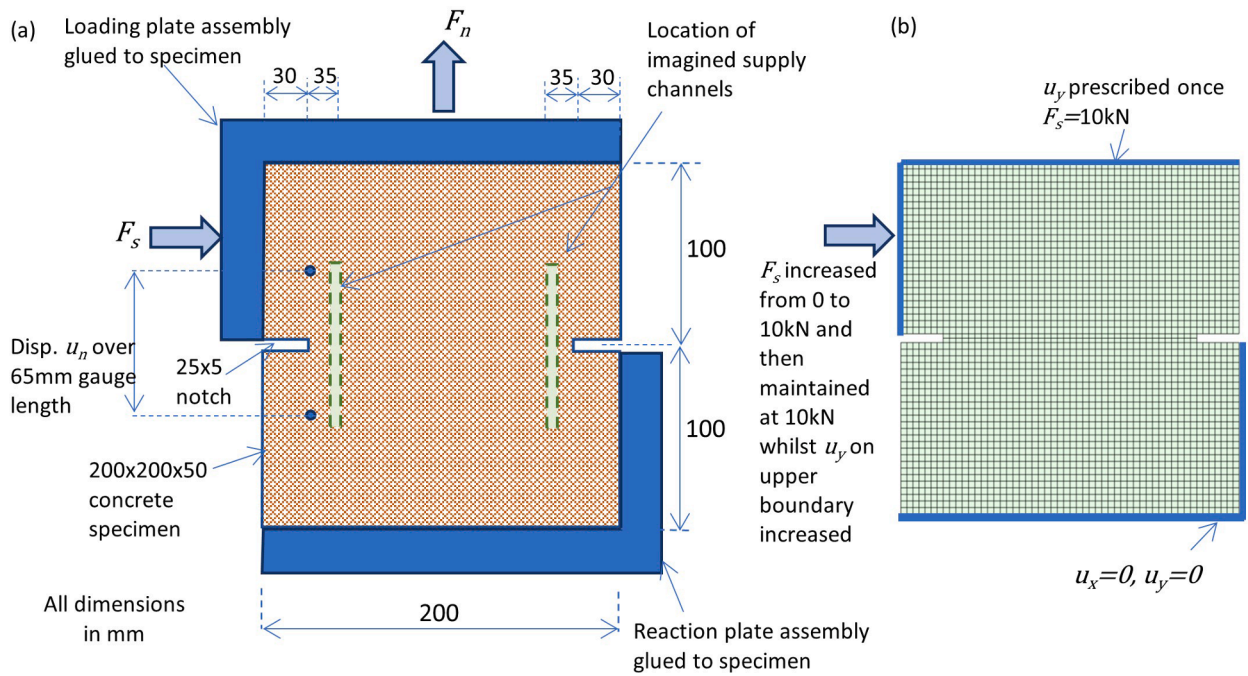
Fig. 11. (a) Experimental arrangement for Nooru-Mohamed test 4b with imagined healing system. (b) FE mesh.
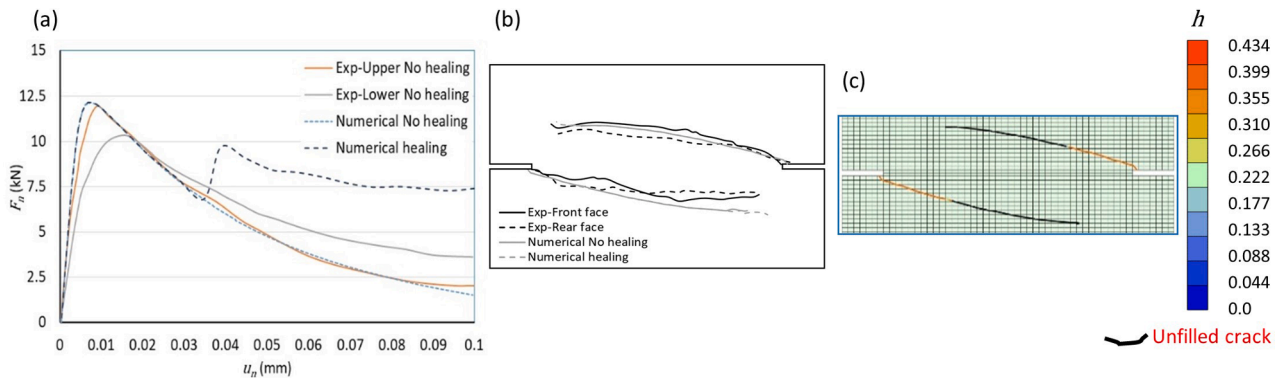

Fig. 12. (a) Experimental and numerical responses. (b) Final experimental and numerical crack patterns. (c) Central part (in height) of the finite element mesh showing the degree of healing at $u_n = 0.039$ mm, $F_n = 9.66$kN.

In addition, for the 60 s and 600 s DT1 cases, results from analyses undertaken using the Evans-Avrami (E-A) healing expression (Section 4) in place of (18) are presented. The results from these simulations, denoted 'Numerical E-A' in Fig. 6a and 6b, show that (18) provides a more accurate representation of the observed healing behaviour than the E-A equation for the partially cured 60 s case. As may be expected, there is less difference between the responses when the healing-agent is fully cured, as in the 600 s DT1 specimens.

We now explore the effect of varying the healing parameters (z_{c0}, τ and z_{c1}) on the post-healing response. The DT1_60s case was selected because the healing-agent is partially cured at this time (60 s), which implies that the response should change with the healing parameters. Fig. 7 shows the effect on the average stress v CMOD response of halving and doubling the values of each of the parameters in turn, relative to those given in Table 3. The graphs show that the healing response is strongly dependent on τ and z_{c0} but that z_{c1} is of second order importance for the parameter range considered here.

The study presented here is contrasted with that we presented in Freeman et al. (2020). The example in the latter gave results for a single healing period and concentrated on showing the ability of the strong discontinuity element to represent crack-healing behaviour using a simplified damage-healing constitutive model. Here, we have explored the effects of healing time, as well as the sensitivity of the computed response to changes in the material parameters, for the cohesive zone model alone.

6.2. Example 2. Notched beam tests for a range of loading rates.

The second example is based on two series of tests on notched concrete beam specimens with embedded channels that were loaded in three-point bending, as illustrated in Fig. 1a. The channels were connected to healing-agent supply tubes that had the facility to be pressurised.

The experiments considered in this example comprise a set of tests from the SF series and three sets of tests from the SO series. In the former (SF tests), each specimen was loaded until the CMOD reached 0.15 mm. The healing-agent supply was then activated and the specimen held at this CMOD for 120 s. Loading was then restarted at a CMOD rate of 0.001 mm/s until the CMOD had reached 0.4 mm, at which point the specimen was unloaded. In the latter (SO tests), the healing-agent supply was activated from the start of the experiment and the load applied so as to maintain a constant CMOD rate once the primary crack had formed.

The SO tests considered here are those with CMOD rates of 0.0005, 0.001 and 0.002 mm/s. All of the SO tests were continued until the CMOD reached 0.3 mm after which the specimens were unloaded. A delivery pressure of 0.5 bar was used for the SO tests; no excess pressure was applied in the SF tests.

The response of the specimens was simulated with the coupled finite element program using two meshes (see Fig. 8). The number of time-steps used for the SO and SF analyses was between 40 and 80, and the point load was applied using prescribed displacements that achieved the required CMOD rate once the primary crack had formed. A lower pre-scribed displacement rate was used in the initial stages to allow the pre-peak response to be captured. The computed meniscus rise response and selected degree of healing results are presented in Fig. 9, and the experimental and numerical load-CMOD responses are given in Fig. 10.

The computed mechanical response for the SF case matches the experimental response with good accuracy, as shown in Fig. 10a. The results from the computations with the two different meshes are suffi-ciently close for the coarser mesh results to be considered mesh converged, and therefore only mesh 1 was used for the SO analyses.

The SF computed meniscus rise response (Fig. 9a) is not compared directly with any experimental data but the numerical results do have the same characteristics as those reported in Gardner et al. (2014) for CA in tapering concrete openings of similar magnitude. For this test, the healing period covered the time interval 100 to 220 s and the meniscus reached a plateau at a height of 60 mm at approximately 112 s. This means that healing took place under static flow and displacement con-ditions from 112 s to 220 s. The results show that this period was suf-ficient for full healing to take place. This conclusion is supported by the results of the full SF experimental series which showed that the exper-imental response did not change appreciably when the healing period was lengthened beyond 2 min (Selvarajoo et al., 2020a).

The numerical predictions for the three SO specimens (Fig. 10b–d) also match the experimental results well and show that the model is able to reproduce the main rate effect in the healing response i.e. that the first healing peak becomes less pronounced and less abrupt as the CMOD rate increases. Fig. 9 shows that the degree of healing through the depth at different times indicates that there is greater healing in the narrower sections but that there are some fluctuations in h near the top of the areas filled with healing-agent resulting from the damage-healing history at these locations. The tendency of the SO responses to reach a load plateau, above that of the corresponding control test, suggests that damage and healing rates balance each other in the latter stages of these tests.

The meniscus rise response (Fig. 9a) is relatively rapid in all cases. The upward movement of the meniscus, after the first plateau, reflects the extension of the primary crack as loading continues and the re-damage of previously healed material. The latter creates a flow path for healing-agent to reach newly cracked sections.

6.3. Example 3. Nooru-Mohamed test 4B reimagined as a healing test

We used experiment 4B (Ref 46–05) from the test series of Nooru-Mohamed (1992) as the basis for the final example. Nooru-Mohamed's tests are well-known and have has been used by a number of in-vestigators to validate their numerical models, e.g. (Cervera and Chiu-menti, 2006). We first considered the original experiment with our numerical model to demonstrate its ability to reproduce the experi-mentally observed behaviour. We then reimagined the experiment as a healing test by assuming that a healing-agent supply system had been introduced into the specimen. The testing arrangement and imagined healing system are given in Fig. 11a, and the finite element mesh, boundary conditions and load path used for the analysis are given in Fig. 11b. As shown, a shear load (F_s) of 10kN was first applied to the upper part of the specimen. Then, while this shear load was maintained at the same value, the upper plate was restrained and displaced in a vertical upward direction with the associated normal load (F_n) being

recorded. In the healing tests, it was assumed that the healing-agent was supplied at no excess pressure and activated once the shear load reached 10kN. A displacement rate of 2.7×10^{-5} mm/s was assumed for the upper surface, which is based on that used in the original experiment and 350 load steps were used in the solution.

The experimental and no-healing numerical responses are compared in Fig. 12a along with a comparison of the experimental and numerical crack patterns in Fig. 12b. The model is able to reproduce the experi-mental behaviour with good accuracy, in terms of both the load–displacement response and the crack path. The contrasting response of the imagined self-healing specimen is shown in Fig. 12a. This shows similar behaviour to that seen in the SO-series notched beams tests, except that there are some minor undulations after the first post-healing peak. The computed degree of healing and the extent of crack filling are shown in Fig. 12c at the first healing peak. At this stage, healing-agent had reached approximately 40% of each crack and some healing has occurred throughout the filled regions.

Although the computed healed response cannot be compared to experimental data, the example illustrates that the model works for multiple curved cracks and gives a credible solution.

6.4. Discussion

The examples show that the coupled model is able to reproduce the major trends observed in the experiments with good accuracy. In particular, the computed responses demonstrate that the new damage-healing model is able to capture the healing dependency on; (i) the COD, as evidenced by the contrasting numerical responses of specimens with different (nominally uniform) CODs (DT1 and DT2) and tapering cracks (SF); (ii) the healing time, which may be seen in the responses of the DT specimens with different healing periods; and (iii) the COD rate, as shown in the SO specimens tested at different displacement rates. The latter also illustrates the ability of the model to simulate the response of structural elements when damage and healing occur simultaneously over a sustained period of time.

The model does not reproduce the multiple healing peaks evident in the experimental SO-series responses. We believe that statistical varia-tions in material strengths across the specimen and a more detailed representation of tortuous crack paths would be required to capture this behaviour.

The damage-healing model, which is the primary subject of this article, has been implemented in 3D although the overall simulations presented here are based on a two-dimensional idealisation. For full 3D simulations, a model that simulates healing-agent flow emanating from channels in curvilinear cracks is required. Such a model has been developed very recently by the authors and will be the subject of a forthcoming article; however, using the 3D flow model in the present examples makes negligible difference to the predicted response and the authors believe that including an account of this 3D flow model would detract from the main message of the paper.

7. Conclusions

Existing models built on continuum-damage-healing-mechanics principles are not able to simulate accurately simultaneous cracking-healing responses in systems that exhibit significant COD and COD-rate effects.

A multi-ligament model of a representative tensile cracking zone, in which the ligament strengths are set according to an appropriate sta-tistical function, can provide valuable insight into the interaction be-tween damage and healing behaviour when healing takes place under continuous crack opening conditions. Simulations undertaken with such a ligament model, for a load case with a constant COD rate, show that discrete blocks of healed material may form over the representative crack area, with the number and size of these blocks tending to increase and decrease respectively as the damage-healing process proceeds.

A consistent set of homogenised damage-healing variables derived from the ligament model results are compatible with a cohesive zone formulation and capture the behavioural crack healing characteristics of a representative zone of SHCM.

The curing of an autonomic healing agent within a discrete crack progresses in the form of two diffuse curing fronts emanating from opposing crack faces. These nonlinear curing fronts may be assumed to be symmetric, with each front progressing in time according to an exponential function. The degree of crack healing may be related to the degree of cure in the overlapping zone between the opposing curing fronts.

A generalised curing front variable, expressed as a convolution integral and updated according to a two-level recursive scheme, is able to capture the curing characteristics within a crack during transient filling, healing, re-cracking and re-healing events.

The application of the curing-front approach in a damage-healing cohesive zone formulation produces a new model that simulates cracking and healing, and naturally accounts for the healing dependency on the COD and its rate.

The implementation of the new cohesive zone model in finite elements with embedded strong discontinuities provides an effective means of simulating the mechanical behaviour of structural components formed from SHCMs.

Overall, the behaviour of autonomic self-healing cementitious materials is governed by a set of interacting mechanical and transport processes. These may be simulated by a coupled finite element model that uses a Navier-Stokes discrete crack-flow model coupled to a mass balance equation for simulating matrix flow, and a combination of the strong-discontinuity element and new damage-healing cohesive model for mechanical behaviour.

A series of validation examples, based on recent experimental work undertaken by the authors' group, as well as data from the literature, show that the coupled model is able to represent the characteristic flow and mechanical behaviour of a vascular self-healing system in a cementitious structural element with good accuracy over a wide range of crack–healing conditions.

Declaration of Competing Interest

The authors declare that they have no known competing financial interests or personal relationships that could have appeared to influence the work reported in this paper.

Appendix A. Damage model functions and standard material properties

The elastic crack-plane constitutive matrix (Section 2.4) is given by:

$$\widetilde{\mathbf{k}}^e = \begin{bmatrix} \widetilde{k}_1 & 0 & 0 \\ 0 & \widetilde{k}_2 & 0 \\ 0 & 0 & \widetilde{k}_3 \end{bmatrix} \tag{A1}$$

where $\widetilde{k}_1 = E_c/h_{fpz}$, $\widetilde{k}_2 = \widetilde{k}_3 = G_c/h_{fpz}$ and G_c is the elastic shear modulus.

The damage evolution and damage surface functions used in Section 3.1 and Section 3.2 are, respectively:

Table A1
Parameters used for ligament and homogenised model comparison (Sections 3.1 and 3.2).

h_{fpz} (mm)	E_c(GPa)	f_t (MPa)	f_{th} (MPa)	τ_h (s)	Δt_h(s)	ζ_m(mm)
50	40	2.0	1.5	60	$\tau_h/3.5$	0.2

$$\omega(\zeta) = 1 - \frac{\zeta_0}{\zeta} e^{-c_1 \frac{\zeta - \zeta_0}{\zeta_m - \zeta_0}} \tag{A2}$$

$$\zeta_{ef}(\widetilde{\mathbf{u}}, \zeta) = \frac{\widetilde{u}_1}{2}\left[1 + \left(\frac{\mu_\zeta}{\gamma_\zeta}\right)^2\right] + \frac{1}{2\gamma_\zeta^2}\sqrt{(\gamma_\zeta^2 - \mu_\zeta^2)^2\widetilde{u}_1^2 + 4\gamma_\zeta^2\left(\widetilde{u}_2^2 + \widetilde{u}_3^2\right)} \tag{A3}$$

where ζ_0 is the damage initiation value of ζ, such that $\zeta_0 = f_t/\widetilde{k}_1^e$, with f_t denoting the tensile strength and $\widetilde{k}_1^e$ the normal elastic stiffness of crack-plane band; ζ_m is the crack opening displacement at the effective end of the softening curve; ω_h takes the same form as (A1) except that ζ_0 and ζ_m are replaced with ζ_{h0} and ζ_{hm} respectively; $\mu_\zeta = \mu_\sigma \frac{E_c}{G_c}, \gamma_\zeta = \gamma_\sigma \frac{E_c}{G_c}, \mu_\sigma = 0.8$ and $\gamma_\sigma = 1.25$. The significance of the latter two parameters and the reason for choosing these values are given in Jefferson and Mihai (2015).

Appendix B. Thermodynamic considerations

We here prove that the crack-plane model predicts non-negative mechanical energy dissipation ($\mathscr{D}$) for any loading cycle. This criterion may be expressed by the Clausius-Duhem inequality (Lemaitre and Desmorat, 2005), as follows:

$$\mathscr{D} = \widetilde{\sigma}^{\mathrm{T}}\dot{\widetilde{\mathbf{u}}} - \dot{\Psi} \geq 0 \tag{B1}$$

where the Helmholtz type energy potential (Ψ) is given by:

$$\Psi = \frac{1}{2}(1 - \omega(\zeta))\widetilde{\mathbf{u}}^{\mathrm{T}}\widetilde{\mathbf{k}}^{\mathrm{e}}\widetilde{\mathbf{u}} + \frac{1}{2}\int_0^t (\widetilde{\mathbf{u}}(t) - \mathbf{u}_{hi}(s))^{\mathrm{T}}\widetilde{\mathbf{k}}^{\mathrm{h}}(\widetilde{\mathbf{u}}(t) - \mathbf{u}_{hi}(s))\frac{\mathrm{d}h(s)}{\mathrm{d}s}\mathrm{d}s \tag{B2}$$

where $\mathbf{u}_{hi}(t) = \widetilde{\mathbf{u}}(t)$ at the moment of healing and it is important to recognise that

$$\Psi \neq \frac{1}{2}(1 - \omega(\zeta))\widetilde{\mathbf{u}}^{\mathrm{T}}\widetilde{\mathbf{k}}^{\mathrm{e}}\widetilde{\mathbf{u}} + \frac{1}{2}h\left(\widetilde{\mathbf{u}} - \widetilde{\mathbf{u}}_h\right)^{\mathrm{T}}\widetilde{\mathbf{k}}^{\mathrm{h}}\left(\widetilde{\mathbf{u}} - \widetilde{\mathbf{u}}_h\right)$$ because of the way $\widetilde{\mathbf{u}}_h$ accumulates during healing.

The elastic matrices $\widetilde{\mathbf{k}}^{\mathrm{e}}$ & $\widetilde{\mathbf{k}}^{\mathrm{h}}$ are symmetric positive definite, such that the quadratic form $\mathbf{y}^{\mathrm{T}}\widetilde{\mathbf{k}}^{\mathrm{e}}\mathbf{y} \geq 0$ for any real valued vector $\mathbf{y}$ (similarly for $\widetilde{\mathbf{k}}^{\mathrm{h}}$) and the damage surface function is convex in stress and relative-displacement space.

Each nonlinear process (damage, re-damage, healing re-healing) is considered in turn and we thereby ensure that the model is valid for each individual process as well as for any combination of these processes.

For virgin damage alone, $\dot{\omega} \geq 0, |\dot{\widetilde{\mathbf{u}}}| \geq 0, \dot{h} = 0$ and $\dot{\mathbf{u}}_h = \mathbf{0}$ and the dissipation reduces to:

$$\mathscr{D}_{dam} = \dot{\omega}\Psi_e \geq 0 \tag{B3}$$

where $\Psi_e = \frac{1}{2}\widetilde{\mathbf{u}}^{\mathrm{T}}\widetilde{\mathbf{k}}^{\mathrm{e}}\widetilde{\mathbf{u}} \geq 0$.

For an increment of virgin healing or re-healing $\dot{h} \geq 0, \left|\dot{\mathbf{u}}_h\right| \geq 0, \dot{\omega} = 0, \dot{\widetilde{\mathbf{u}}} = 0$ and the dissipation, from (B1) and (B2), becomes:

$$\mathscr{D}_{heal}(t) = -\dot{\Psi} = \frac{1}{2}\widetilde{\mathbf{u}}(t)^{\mathrm{T}}\widetilde{\mathbf{k}}^{\mathrm{h}}\widetilde{\mathbf{u}}(t) + \frac{1}{2}\mathbf{u}_{hi}(t)^{\mathrm{T}}\widetilde{\mathbf{k}}^{\mathrm{h}}\mathbf{u}_{hi}(t) - \frac{2}{2}\widetilde{\mathbf{u}}(t)^{\mathrm{T}}\widetilde{\mathbf{k}}^{\mathrm{h}}\mathbf{u}_{hi}(t) \tag{B4}$$

since $\mathbf{u}_{hi}(t) = \widetilde{\mathbf{u}}(t)$, $\mathscr{D}_{heal}(t) = 0$.

When only re-damage occurs, we set $\left|\dot{\widetilde{\mathbf{u}}}\right| \geq 0, \dot{\omega}_h \geq 0, \dot{h}_v = \dot{\omega} = 0, \dot{\mathbf{u}}_h = 0$ and make use of (9) to derive the following expression for the dissipation;

$$\mathscr{D}_{redam} = \dot{\omega}_h\Psi_{re} \geq 0 \tag{B5}$$

where $\Psi_{re} = \frac{1}{2}\int_0^t (\widetilde{\mathbf{u}}(t) - \mathbf{u}_{hi}(s))^{\mathrm{T}}\widetilde{\mathbf{k}}^{\mathrm{h}}(\widetilde{\mathbf{u}}(t) - \mathbf{u}_{hi}(s))\mathrm{d}s \geq 0$.

Appendix C. Transport and curing models with associated material parameters

Transport model

The governing equations for the discrete crack flow are as follows (Freeman and Jefferson, 2020):

$$\frac{\partial(\rho\dot{\chi})}{\partial t} + \dot{\chi}\frac{\partial(\rho\dot{\chi})}{\partial\chi} = -\frac{\partial P_{hcrk}}{\partial\chi} - \eta\dot{\chi} - \rho\dot{\chi}q_{crk} + \rho g sin(\psi) \quad \text{in } \Omega_{crk}$$

$$\frac{\partial(\rho w_c)}{\partial t} + \frac{\partial(\rho w_c\dot{\chi})}{\partial\chi} + \rho w_c q_{crk} = 0 \text{ in } \Omega_{crk}$$

$$P_{hcrk} = -P_{c0}(1 - \beta_s) + \frac{2\beta_m\dot{\chi}_m}{w_c} \text{ on } \Gamma_m \tag{C1}$$

$$P_{hcrk} = P_a \text{ on } \Gamma_d$$

where Ω_{crk} indicates the crack domain, Γ_m and Γ_d denote the meniscus and the part of the boundary where pressure is prescribed respectively; β_m and β_s are meniscus and stick slip material parameters, P_{hcrk} is the healing-agent pressure in the crack, ψ is the crack inclination and ρ is the healing-agent density; the dependent functions are given in Table C1.

The governing equations for the matrix flow are as follows:

$$\frac{\partial(\overline{\rho_h})}{\partial t} + \nabla \bullet \mathbf{J}_{\mathrm{h}} + \rho q_{mtx} = 0 \quad \text{in } \Omega_{mtx}$$

$$\overrightarrow{\mathbf{n}} \bullet \mathbf{J}_{\mathrm{h}} = q_c \quad \text{on } \Gamma_{Nf} \tag{C2}$$

where Ω_{mtx} defines the cementitious domain, Γ_{Nf} is the part of the boundary where the flux is prescribed and $\overrightarrow{\mathbf{n}}$ is a unit vector on the boundary; $\overline{\rho_h} = \rho n S_h$ is the phase averaged density, S_h is the degree of CA saturation, and dependent functions and associated parameters are given in Table C1.

Table C1

Transport model constitutive relationships from (Freeman and Jefferson, 2020).

Constitutive relationship description	Mathematical relationship	Parameters / dependent variables
Meniscus contact angle	$\theta_m(C_a) = acos(cos(\theta_{m0}) - (cos(\theta_{m0}) + 1) tanh(c_1 C_a^{c_2}))$ (C3)	$C_a = \mu \dot{\chi}_m / \gamma$ = capillary number, γ = surface tension, $c_1 = 1.325$ and $c_2 = 0.350$. χ is the convected coordinate along the crack
HA viscosity	$\mu = \mu_0 \left(\dfrac{\phi_g}{\phi_g - \phi}\right)^{n_v}$ (C4)	μ_0 is the initial viscosity, ϕ_g is the degree of cure at the gel point and n_v is an exponent
Sink source term	$q_{crk} = \dfrac{2}{\rho} n \beta_{crk}(P_{hcrk} - P_h) = -q_{mtx}$ (C5)	β_{crk} = boundary transfer coefficient, ρ = CA density, n= matrix porosity, and P_{hcrk} and P_h are the crack and matrix pressures respectively.
Young-Laplace capillary pressure for HA in a discrete crack	$P_{c0} = \dfrac{2\gamma cos(\theta_m - \vartheta)}{w_c}$ (C6)	γ is the surface tension ϑ is the inclination of the crack wall
Effective viscosity	$\eta = \dfrac{\mu}{k + 0.5\mu w_c \beta_w \beta_{wr}}$ (C7)	$k = w_c^2/12$; β_w is a wall slip factor $\beta_{wr} = 1 - (\varphi_{xc}/\varphi_g)^{nv}$ φ_{xc} is the wall degree of cure
Minimum crack opening that HA can enter a crack	$w_{cmin} = AP_a + B$ (C8)	$A = -0.014\dfrac{mm}{bar}; B = 0.015mm.$
HA pressure	$P_h = P_g - P_c$ (C9)	P_g is the gas pressure (assumed to be atmospheric)
HA flux in matrix	$\mathbf{J}_h = -\rho K_{eff}(S_h)(\nabla P_h - \rho \mathbf{g})$ (C10)	K_{eff}, effective diffusion (see C12)
Matrix capillary pressure	$P_{c0} = a\left(S_h^{-\frac{1}{m}} - 1\right)^{1-m}$ (C11)	a and m are constants that depend on the medium (see Table C2).
Effective diffusion coefficient & relative permeability	$K_{eff} = \dfrac{K_{int} K_{hrel}(S_h)}{\mu}$ (C12) $K_{hrel} = S_h^{\lambda}\left[1 - \left(1 - S_h^{\frac{1}{m}}\right)^m\right]^2$ (C13)	λ is the pore interaction factor (see Table C2)

[1]HA = healing-agent.

Table C2

Transport model parameters.

Parameter	Value	Parameter	Value	Parameter	Value	Parameter	Value
$K_{int}(m^2)$	3×10^{-17}	$a(N/m^2)$	1.86×10^7	$\varphi_g(-)$	1	$\gamma(N/m)$	0.033
$n(-)$	0.12	$m(-)$	0.44	$nv(-)$	2.193	$\beta_m(Ns/m^2)$	0
$\rho(kg/m^3)$	1060	$\lambda(-)$	‑3	$\beta_{crk}(s/m)$	1×10^{-11}	$\beta_s(-)$	0
$\mu(Ns/m^2)$	0.004	$\tau_m(s)$	28.5	$\theta_{m0}(rad)$	0.17543	$\beta_w(m^3/Ns)$	0.005

In the present study, stability of the crack flow model is ensured using a continuous interior penalty, whilst a quasi-mass lumped storage matrix approach is employed for the matrix flow model. The transport model parameters used in the simulations are given in Table C2.

Further background to the curing model

Eqs. (1) and (2) are applicable to the curing of a body of CA when the thickness is relatively thin (<1mm) and the spread dimensions are at least an order of magnitude greater than the thickness. For larger thicknesses of healing-agent, thermal convection can become significant (Li et al., 2017) and a modification may be required to both equations (1) and (2). Since, the thickness of the cracks considered in this work do not exceed 0.4 mm, equations (1) and (2) are considered appropriate for the examples presented in Section 6. However, the thickness of the layer of CA used in our curing characterisation experiments (Selvarajoo et al., 2020b) was 6 mm and thus thermal convection is likely to have had an influence on the curing response in these tests. We have allowed for this in an approximate way by using a larger value of z_{c0} for the comparison shown in Fig. 2a than that used for the Section 6 examples. The material parameters used for the theoretical curve in Fig. 2 were as follows: $\tau = 60$ s, $z_{c0} = 0.3$ mm, $z_{c1} = 25$ mm, $z_{c2} = 0.0001$ mm.

References

Alsheghri, A.A., Abu Al-Rub, R.K., 2015. Thermodynamic-based cohesive zone healing model for self-healing materials. Mech. Res. Commun. 70, 102–113. https://doi.org/10.1016/j.mechrescom.2015.10.003.

Barbero, E.J., Greco, F., Lonetti, P., 2005. Continuum damage-healing mechanics with application to self-healing composites. Int. J. Damage Mech. 14, 51–81. https://doi.org/10.1177/1056789505045928.

Caggiano, A., Etse, G., Ferrara, L., Krelani, V., 2017. Zero-thickness interface constitutive theory for concrete self-healing effects. Comput. Struct. 186, 22–34. https://doi.org/10.1016/j.compstruc.2017.02.005.

Cervera M, Chiumenti M. 2006. Smeared crack approach: back to the original crack. International Journal for Numerical and Analytical Methods in Geomechanics. 30, 1173–1199. (doi:/.org/10.1002/nag.518).

Darabi, M.K., Abu Al-Rub, R.K., Little, D.N., 2012. A continuum damage mechanics framework for modeling micro-damage healing. Int. J. Solids Struct. 49, 492–513. https://doi.org/10.1016/j.ijsolstr.2011.10.017.

Davies, R.E., Jefferson, A.D., 2017. Micromechanical modelling of self-healing cementitious materials. Int. J. Solids Struct. 113–114, 180–191. https://doi.org/10.1016/j.ijsolstr.2017.02.008).

De Belie, N., Gruyaert, E., Al-Tabbaa, A., Antonaci, P., Baera, C., Bajāre, D., Darquennes, A., Davies, R., Ferrara, L., Jefferson, T., Litina, C., Miljevic, B., Otlewska, A., Ranogajec, J., Roig, M., Paine, K., Pawel, L., Serna, P., Tulliani, J.M., Vucetic, S., Wang, J., Jonkers, H., 2018. A review on self-healing concrete for damage management of structures. Adv. Mater. Interfaces 5, 1–28. https://doi.org/10.1002/admi.201800074.

De Borst R, Crisfield MA, Remmers JRC, Verhoosel CV. 2012. Nonlinear Finite Element Analysis of Solids and Structures, Wiley, ISBN: 978-0-470-66644-9.

De Maio, U., Cendón, D., Greco, F., Leonetti, L., Nevone Blasi, P.N., Planas, J., 2021. Investigation of concrete cracking phenomena by using cohesive fracture-based techniques: a comparison between an embedded crack model and a refined diffuse interface model. Theor. Appl. Fract. Mech. 103062 https://doi.org/10.1016/j.tafmec.2021.103062.

De Nardi C, Gardner D, Jefferson AD. 2020. Development of 3D printed networks in self-healing concrete. Materials 13(6), article number: 1328. (doi: /10.3390/ma13061328).

Dry, C., 1994. Matrix cracking repair and filling using active and passive modes for smart timed release of chemicals from fibres into cement matrices. Smart Mater. Struct. 3 (2), 118–123.

Elices, M., Guinea, J., Gómez, J., Planas, J., 2002. The cohesive zone model: advantages, limitations and challenges. Eng. Fract. Mech. 69 (2), 137–163. https://doi.org/10.1016/S0013-7944(01)00083-2.

Ferrara, L., Van Mullem, T., Alonso, M.C., Antonaci, P., Borg, R.P., Cuenca, E., Jefferson, A., Ng, P.-L., Peled, A., Roig-Flores, M., Sanchez, M., Schroefl, C., Serna, P., Snoeck, D., Tulliani, J.M., De Belie, N., 2018. Experimental characterization of the self-healing capacity of cement based materials and its effects on the material performance: a state of the art report by COST Action SARCOS WG2. Constr. Build. Mater. 167, 115–142. https://doi.org/10.1016/j.conbuildmat.2018.01.143.

Freeman B, Jefferson A. 2020. The simulation of transport processes in cementitious materials with embedded healing systems. International Journal for Numerical and Analytical Methods in Geomechanics 44(2), pp. 293-326. (doi:10.1002/nag.3017).

Freeman BL, Bonilla-Villalba P, Mihai IC, Alnaas WF, Jefferson AD. 2020. A specialised finite element for simulating self-healing quasi-brittle materials. Adv. Model. and Simul. in Eng. Sci. 7 32 (doi: 10.1186/s40323-020-00171-4).

Gardner D, Herbert D, Jayaprakash M, Jefferson AD, Paul A. 2017. Capillary flow characteristics of an autogenic and autonomic healing-agent for self-healing concrete. Journal of Materials in Civil Engineering, ASCE 29(11). (doi:10.1061/(ASCE)MT.1943-5533.0002092).

Gardner, D., Jefferson, A.D., Hoffman, A., Lark, R., 2014. Simulation of the capillary flow of an autonomic healing-agent in discrete cracks in cementitious materials. Cem. Concr. Res. 58, 35–44. https://doi.org/10.1016/j.cemconres.2014.01.005.

Gardner, D., Lark, R., Jefferson, T., Davies, R., 2018. A survey on problems encountered in current concrete construction and the potential benefits of self-healing cementitious materials. Case Stud. Constr. Mater. 8, 238–247. https://doi.org/10.1016/j.cscm.2018.02.002.

Gilabert, F.A., Garoz, D., Van Paepegem, W., 2017a. Macro-and micro-modeling of crack propagation in encapsulation-based self-healing materials: application of XFEM and cohesive surface techniques. Mater. Des. 130, 459–478. https://doi.org/10.1016/j.matdes.2017.05.050.

Gilabert, F.A., Van Tittelboom, K., Van Stappen, J., Cnudde, V., De Belie, N., Van Paepegem, W., 2017b. Integral procedure to assess crack filling and mechanical contribution of polymer-based healing-agent in encapsulation-based self-healing concrete. Cem. Concr. Compos. 77, 68–80. https://doi.org/10.1016/j.cemconcomp.2016.12.001.

Gitman, I.M., Askes, H., Sluys, L.J., 2007. Representative volume: Existence and size determination. Eng. Fract. Mech. 74, 2518–2534. https://doi.org/10.1016/j.engfracmech.2006.12.021.

Granger S, Pijaudier-Cabot G, Loukili A. 2007. Mechanical behaviour of self-healed ultra high performance concrete: from experimental evi-dence to modeling. Proceedings of the 6th international conference on fracture mechanics of concrete and concrete structures. 3:1827-1834.

Han, K.J., Ju, W., Zhang, H., Zhu, Y., Chang, T.-S., Wang, Z., 2021. Mechanical response analysis of self-healing cementitious composites with microcapsules subjected to tensile loading based on a micromechanical damage-healing model. Constr. Build. Mater. 280, 122251 https://doi.org/10.1016/j.conbuildmat.2021.122251.

Jefferson AD. 2002. Tripartite cohesive crack model. ASCE Journal of engineering mechanics 128 (6), 644-653. (doi:10.1061/(ASCE)0733-9399(2002)128:6(644)).

Jefferson, A.D., Mihai, I.C., 2015. The simulation of crack opening-closing and aggregate interlock behaviour in finite element concrete models. Int. J. Numer. Meth. Eng. 104 (1), 48–78. https://doi.org/10.1002/nme.4934.

Jefferson, T., Javierre, E., Freeman, B., Zaoui, A., Koenders, A., Ferrara, L., 2018. Research progress on numerical models for self-healing cementitious materials. Adv. Mater. Interfaces 5, 1–19. https://doi.org/10.1002/admi.201701378.

Joseph, C., Jefferson, A., Isaacs, B., Lark, R., Gardner, D., 2010. Experimental investigation of adhesive-based self-healing of cementitious materials. Mag. Concr. Res. 62 (11), 831–843. https://doi.org/10.1680/macr.2010.62.11.831.

Krajcinovic, D., 1996. Damage mechanics. North-Holland, Amsterdam.

Lemaitre J, Desmorat R. 2005. Engineering Damage Mechanics. Springer (ISBN 3-540-21503-4).

Li, Y.J., Barthès-Biesel, D., Salsac, A.V., 2017. Polymerization kinetics of n-butyl cyanoacrylate glues used for vascular embolization. J. Mech. Behav. Biomed. Mater. 69, 307–317. https://doi.org/10.1016/j.jmbbm.2017.01.003.

Mauludin, L.M., Oucif, C., 2019. Modeling of self-healing concrete: a review. J. Appl. Comput. Mech. 5 (3), 526–539. https://doi.org/10.22055/jacm.2017.23665.1167.

Mergheim, J., Steinmann, P., 2013. Phenomenological modelling of self-healing polymers based on integrated healing-agents. Comput. Mech. 52 (3), 681–692. https://doi.org/10.1007/s00466-013-0840-0.

Minnebo, P., Thierens, G., De Valck, G., Van Tittelboom, K., De Belie, N., Van Hemelrijck, D., Tsangouri, E., 2017. A novel design of autonomously healed concrete: Towards a vascular healing network. Materials 10, 1–23. https://doi.org/10.3390/ma10010049.

Nooru-Mohamed, M.B., 1992. Mixed-Mode Fracture of Concrete: An Experimental Approach. Delft University of Technology, The Netherlands. PhD Thesis.

Oucif, C., Voyiadjis, G.Z., Rabczuk, T., 2018. Modeling of damage-healing and nonlinear self-healing concrete behavior: Application to coupled and uncoupled self-healing mechanisms. Theor. Appl. Fract. Mech. 96, 216–230. https://doi.org/10.1016/j.tafmec.2018.04.010.

Pan, Y., Tian, F., Zhong, Z., 2018. A continuum damage-healing model of healing-agents based self-healing materials. Int. J. Damage Mech. 27 (5), 754–778. https://doi.org/10.1177/1056789517702211.

Schimmel EC, Remmers JJC. 2006. Development of a constitutive model for self-healing materials. Delft Aerospace Computational Science, Report DACS-06-003.

Selvarajoo, T., Davies, R.E., Freeman, B.L., Jefferson, A.D., 2020a. Mechanical response of a vascular self-healing cementitious material system under varying loading conditions. Constr. Build. Mater. 254, 119245 https://doi.org/10.1016/j.conbuildmat.2020.119245.

Selvarajoo, T., Davies, R.E., Gardner, D.R., Freeman, B.L., Jefferson, A.D., 2020b. Characterisation of a vascular self-healing cementitious materials system: flow and curing properties. Constr. Build. Mater. 245, 118332 https://doi.org/10.1016/j.conbuildmat.2020.118332.

Simo, J.C., Hughes, T.J.R., 1998. Computational Inelasticity. Springer.

The Royal Society, 2021. Animate Materials. The Royal Society, London, UK.

Tomlinson, S.K., Ghita, O.R., Hooper, R.M., Evans, K.E., 2006. The use of near-infrared spectroscopy for the cure monitoring of an ethyl cyanoacrylate adhesive. Vib. Spectrosc. 40 (1), 133–141. https://doi.org/10.1016/j.vibspec.2005.07.009.

Van Belleghem, B., Van Tittelboom, K., De Belie, N., 2018. Efficiency of self-healing cementitious materials with encapsulated polyurethane to reduce water ingress through cracks. Materiales de Construcción 68. https://doi.org/10.3989/mc.2018.05917.

Van Tittelboom K, De Belie N. 2013. Self-healing in cementitious materials-a review. Materials (Basel), 6(6), 2182-2217. (doi:10.3390/ma6062182).

Voyiadjis GZ, Shojaei A, Li G, Kattan PI. 2012. A theory of anisotropic healing and damage mechanics of materials. Proceedings of the Royal Society, A – Mathematical, Physical, and Engineering Sciences 468(2137), 163–183. (:doi/10.1098/rspa.2011.0326).

Voyiadjis, G.Z., Shojaei, A., Li, G., 2011. A thermodynamic consistent damage and healing model for self healing materials. Int. J. Plast. 27 (7), 1025–1044. https://doi.org/10.1016/j.ijplas.2010.11.002.

White, S.R., Sottos, N.R., Geubelle, P.H., Moore, J.S., Kessler, M.R., Sriram, S.R., Brown, E.N., Viswanathan, S., 2001. Autonomic healing of polymer composites. Nature 409, 794–797. https://doi.org/10.1038/35057232.

Wool, R.P., O'Connor, K.M., 1981. A theory of crack healing in polymers. J. Appl. Phys. 52, 5953–5963.

Xue, C., Li, W., Li, J., Tam, V.W.Y., Ye, G., 2019. A review study on encapsulation-based self-healing for cementitious materials. Struct. Concr. 20, 198–212. https://doi.org/10.1002/suco.201800177.

Zhang, Y., Zhuang, X., 2018. A softening-healing law for self-healing quasi-brittle materials: analyzing with strong-discontinuity embedded approach. Eng. Fract. Mech. 192, 290–306. https://doi.org/10.1016/j.engfracmech.2017.12.018.

Zhou, S., Zhu, H., Ju, J.W., Yan, Z., Chen, Q., 2017. Modeling microcapsule-enabled self-healing cementitious composite materials using discrete element method. Int. J. Damage Mech. 26, 340–357. https://doi.org/10.1177/1056789516688835.

Zienkiewicz OC, Taylor RL, Fox D. 2014. The Finite Element Method for Solid and Structural Mechanics Butterworth-Heinemann. (doi: /10.1016/C2009-0-26332-X).